Ozone vertical distribution in Mars Years 27–30 from SPICAM/MEX UV occultations

Anni Määttänen, Franck Lefèvre, Loïc Verdier, Franck Montmessin, Constantino Listowski, Sabrina Guilbon, Anna Fedorova, Oleg Korablev

Ozone vertical distribution in Mars Years 27-30 from SPICAM/MEX UV occultations

A Määttänen[a,*], F. Lefèvre[a], L. Verdier[b], F. Montmessin[b], C. Listowski[b,1], S. Guilbon[b,2], A. Fedorova[e] and O. Korablev[e]

[a]LATMOS/IPSL, Sorbonne Université, UVSQ Université Paris-Saclay, CNRS, Paris, France
[b]LATMOS/IPSL, UVSQ Université Paris-Saclay, Sorbonne Université, CNRS, Guyancourt, France
[e]Space Research Institute (IKI) RAS, Moscow, Russian Federation

ARTICLE INFO

Keywords:
Mars, atmosphere
Atmospheres, structure
Ultraviolet observations
Occultations

ABSTRACT

The SPICAM/MEX ultraviolet spectrometer probed the Martian atmosphere with the occultation method from 2004 until 2014. SPICAM/MEX performed both stellar and solar occultations during in total four Martian Years with good spatial and seasonal coverages. We have analyzed these occultations and performed a rigorous quality check of the retrievals to eliminate false detections. We present the observed features of the vertical distribution of Martian ozone, a key chemical species. Stellar occultations probe the nightside atmosphere, whereas solar occultations are acquired at the terminator (sunrise or sunset), enabling the study of the day-night transition of this photochemically active species. Comparison of the observations with a global climate model show a good overall agreement. However, quantitative differences are found in certain regions, possibly related to difficulties in correct modeling of the water cycle. Our dataset allows us to study certain particular features of Martian ozone. The low- and midlatitude ozone layer forming during northern spring is mapped in both hemispheres and its night-terminator variations are probed with the combination of stellar and solar occultations. The southern polar winter vortex shows hints of the well-known mid-altitude ozone layer already detected previously. During the northern polar spring, SPICAM observes the top of the lower atmosphere ozone layer above 10 km, showing O_3 concentrations that the model reproduces quite well. SPICAM observations are in good agreement with previously published observations from other instruments.

1. Introduction

Ozone (O_3) on Mars is a by-product of the photolysis of CO_2, producing the O atoms that are necessary for the well-known reaction:

$$O + O_2 + CO_2 \longrightarrow O_3 + CO_2. \quad (1)$$

During the day, the main loss of O_3 is photolysis, which occurs at a timescale shorter than five minutes at all altitudes:

$$O_3 + h\nu \longrightarrow O(^1D) + O_2. \quad (2)$$

The oxygen atoms produced by photolysis in their excited state $O(^1D)$ are then rapidly quenched by CO_2 to return to their ground state, here noted O for simplicity. All the reactions of exchange between O, $O(^1D)$ and O_3 are fast. Thus, each of these species can therefore be considered in photochemical equilibrium within the so-called O_x family ($O_x = O(^1D) + O + O_3$). For instance, the loss of O_3 through photolysis does not represent a net loss of O_x since atomic oxygen produced in Eq. (2) recombines immediately with O_2 to reform O_3.

*Corresponding author
anni.maattanen@latmos.ipsl.fr (A. Määttänen); franck.lefevre@latmos.ipsl.fr (F. Lefèvre); loic.verdier@latmos.ipsl.fr (L. Verdier); franck.montmessin@latmos.ipsl.fr (F. Montmessin); constantino.listowski@cea.fr (C. Listowski); sabrina.guilbon@protonmail.com (S. Guilbon); fedorova@iki.rssi.ru (A. Fedorova); korab@iki.rssi.ru (O. Korablev)
ORCID(s):
[1]Currently at: CEA/DAM/DIF, F-91297 Arpajon, France
[2]Currently at: Dennemeyer & Co. Sàrl, Luxembourg

During the day, the loss of O_x in the atmosphere of Mars is known to take place through various reactions with the hydrogen radicals H, OH, HO_2 (i.e., the HO_x family) produced by the dissociation of H_2O and H_2 (e.g., see Lefèvre and Krasnopolsky, 2017, for a review). In the presence of H_2O, the loss of O_x occurs with a short timescale of typically 1 hour below 25 km. Due to the strong pressure dependence of the three-body reaction (1), O_3 is the main form of O_x at those altitudes. Thus, there is a tight coupling between daytime O_3 and HO_x species and O_3 can be considered as a sensitive tracer of the HO_x chemistry that regulates the composition of the CO_2 atmosphere of Mars. For that reason, and because O_3 is more easily detectable than H, OH, or HO_2, ozone has received considerable interest since its discovery on Mars in the early 1970s (Barth and Hord, 1971; Barth et al., 1973). However, it should be mentioned that a member of the HO_x family, H_2O_2, has been detected on Mars (Clancy et al., 2004; Encrenaz et al., 2004). During nighttime, the ozone chemistry is much less active due to the lower concentrations of HO_x (Munoz et al., 2005; Cariolle et al., 2017) but nighttime O_3 concentrations are nevertheless determined by the amount of O_x remaining at sunset.

There has been significant progress in recent years in the knowledge of the O_3 climatology on Mars, in particular thanks to the data collected in the ultraviolet range with the instrument SPectroscopie pour l'Investigation des Caractéristiques Atmosphériques de Mars on Mars Express (SPICAM/MEX) (Perrier et al., 2006; Willame et al., 2017; Lefèvre et al., 2021) and the Mars Color Imager on Mars Reconnaissance Orbiter (MARCI/MRO) (Clancy et al., 2016) spaceborne instruments. However, these daytime observations performed in nadir geometry can only retrieve the ozone integrated column, which is mostly representative of the lower atmosphere where the O_3 number density is largest and has little diurnal variability.

Knowledge of the ozone vertical profile gives access to more elevated regions of the atmosphere where ozone is expected to undergo strong seasonal variations driven by the variation of the hygropause altitude between Mars aphelion and perihelion (Clancy and Nair, 1996; Lefèvre et al., 2004). In addition, above 25 km, reaction (1) becomes less efficient and O becomes the dominant species in the O_x family during the day, at the expense of O_3. Ozone reforms in large quantities at night via reaction (1) in the absence of photolysis (reaction 2). In contrast to the lower atmosphere, strong day/night variations of ozone are therefore expected in the middle and upper atmosphere of Mars. These dramatic diurnal and seasonal variations of O_3 in the middle and upper atmosphere offer a powerful constraint for photochemical models. However, measurements of the O_3 vertical profile were rare for a long time: during the day, only few uncertain O_3 profiles were obtained at the same season (L_s = 10-15°) from the Mars 5 (Krasnopolsky and Parshev, 1979) and Phobos 2 (Blamont and Chassefiere, 1993) spacecrafts. Daytime measurements of $O_2(^1\Delta_g)$ emission profiles by Guslyakova et al. (2014) and Clancy et al. (2017) can also provide an indirect estimation of ozone concentrations. Guslyakova et al. (2014) compared the observed and modeled $O_2(^1\Delta_g)$ distributions and concluded that detailed modeling of water ice cloud microphysics was necessary for a good model prediction of the $O_2(^1\Delta_g)$ emission, but they did not discuss ozone distributions in their paper. The Clancy et al. (2017) retrievals were the first extensive dataset that also gave insight into the daytime behavior of ozone vertical distribution. A handful of SPICAM solar occultations were published by Piccialli et al. (2021) in a study testing the effect on the retrievals of accounting for the horizontal atmospheric gradients at the terminator. The ExoMars Trace Gas Orbiter has been observing the Martian atmosphere in solar occultation for some years now and the first ozone profiles at the solar terminator have been recently published (Olsen, K. S. et al., 2020; Khayat et al., 2021; Patel et al., 2021b). At night, the first and most extensive dataset of the ozone vertical distribution was presented by Lebonnois et al. (2006). Their data were obtained by SPICAM/MEX stellar occultation and covered almost three quarters of a Martian year (L_s = 8-270°). Lebonnois et al. (2006) reported on the aphelion season ozone layer above the hygropause (around 30 km) and the near-surface layer of ozone in the Southern polar winter. They also detected a layer around 50 km altitude in the Southern polar night, later on studied more in detail by Montmessin and Lefèvre (2013). Montmessin and Lefèvre (2013) focused solely on the Southern polar night with SPICAM stellar occultations available at the time, and explained the Southern polar winter ozone layer at 50 km as a result of recombination of oxygen atoms transported by the mean meridional circulation from sunlit lower latitudes. Recently, the stellar occultation technique was also used by Gröller et al. (2018) to derive nighttime O_3 profiles between 20 km to 60 km from the MAVEN/IUVS ultraviolet spectrometer. Their data covers 12 week-long periods evenly sampled in a two Martian year timeframe, and they present 18 ozone profiles (out of 70 occultations with O_3 detection). Gröller et al. (2018) reported measurements of the aphelion ozone layer in northern late spring and southern midwinter, and large amounts of ozone in the lowest 30 km of the atmosphere at high southern latitudes in early southern fall. Overall, the features observed in IUVS ozone profiles of Gröller et al. (2018) and in SPICAM results of Lebonnois et al. (2006) are qualitatively in agreement, but there is a factor of 2 to 5 difference in the measured concentrations, IUVS measuring less ozone than SPICAM (Gröller et al., 2018).

We present here the first terminator-nighttime climatology of the ozone vertical distribution on Mars. The ozone

profiles have been retrieved from both SPICAM/MEX solar and stellar occultations, and cover just over four Martian years. At night, our work extends the study of Lebonnois et al. (2006) that only pertained to the first 3/4 of a Martian year of operation of SPICAM/MEX and the subset of data used by Montmessin and Lefèvre (2013) who focused on the Southern polar winter atmosphere only. The combination of the two occultation types reveals a part of the ozone diurnal variation. The ozone detections have been screened with very strict detection criteria that remove false detections often encountered in very aerosol-laden situations (near the surface and during the second half of the Martian year) but also due to other reasons related to data quality. The data presented in this paper constitute the reference SPICAM ozone vertical distribution dataset.

2. Methods

2.1. SPICAM/MEX ultraviolet occultations

To probe the vertical distribution of O_3, we employ the UV occultations of SPICAM/MEX. SPICAM/MEX is an ultraviolet and near-infrared spectrometer, described in detail by Bertaux et al. (2006), capable of detecting the ozone absorption centered around 255 nm with its ultraviolet channel that covers the range from 118 nm to 320 nm.

The retrieval method and the first analyses of the stellar occultations in the UV concerning aerosol, ozone and temperature profiles have been described by Quémerais et al. (2006), Montmessin et al. (2006), Lebonnois et al. (2006) and Forget et al. (2009). Another study on ozone using stellar occultations, focused on the polar regions, was published by Montmessin and Lefèvre (2013). The solar occultations in the UV were analyzed, for the first time, by Määttänen et al. (2013) who presented aerosol profile retrievals.

During an occultation, the instrument is pointed towards a light source (a star or the Sun) and is kept in this inertial attitude while the satellite moves along its orbit, recording spectra while the light source sets behind or rises from behind the planet. The measurements start/end well above the dense part of the atmosphere (above 120 km) so that the light source spectrum free of any atmospheric extinction can be recorded, providing a reference spectrum for every individual occultation measurement. It should be noted that occultations can not probe very well the near-surface atmosphere due to signal loss because of increasing aerosol opacity. The vertical resolution of SPICAM occultations is determined by the instrument's sampling frequency, leading to a resolution of about 1-3 km (Montmessin et al., 2006).

Our dataset consists of 1793 stellar occultations and 541 solar occultations acquired mainly from end of Mars Year (MY) 26 through MY31. These correspond to orbits between 00174A03 and 10952A01 (acquisition dates between March 5, 2004 and August 7, 2012). The UV channel of SPICAM started experiencing problems in the end of 2011 and ceased operations in 2014. Ozone detection (using our selection criteria, see Section 2.3) was confirmed in 487 stellar and 160 solar occultations.

The presented altitudes in this paper are altitudes above the areoid. The spatio-temporal coordinates (latitude, longitude, local time, solar longitude) of an occultation are given for the line-of-sight at tangent altitude of 85 km (these coordinates naturally vary slightly during the course of an occultation).

2.2. Retrieval method

We refer the interested reader to Quémerais et al. (2006), Montmessin et al. (2006) and Määttänen et al. (2013) for a complete description of the instrument, the observation mode and the analysis methods of both occultation types, and we only recall the main points here with a focus on features specific to this study. Montmessin et al. (2017) give also a good overview of the SPICAM instrument and the data analysis along with a review of its main achievements.

The occultation method allows for the retrieval of absolute quantities from relative spectra (transmittances). For calculating the atmospheric transmittances, a reference spectrum of the light source is assembled from a collection of spectra acquired above the atmosphere. This reference is then used to normalize the spectra measured while the line-of-sight (LOS) traverses the atmosphere, producing transmittances. These transmittance spectra reveal the characteristic absorption bands of atmospheric gaseous species and the continuum attenuation by aerosol particles. Each individual observation is normalized by its own reference spectrum, making most of the calibration procedure insensitive to potential drifts in measurement absolute calibration, since the normalization intrinsically accounts for any changes in the instrument over time.

From orbit 1776 (June 4, 2005) onwards the solar occultations suffered from pointing oscillations caused by the MARSIS radar antenna: the procedure to eliminate these oscillations from the spectra, as well as other details related to the solar occultation data reduction, are described in detail in Määttänen et al. (2013).

SPICAM UV transmittance spectra can be modeled with the Beer-Lambert law by accounting for the absorbing gaseous species (CO_2 and O_3) and the aerosol extinction, for which we use the so called α-model (O'Neill and Royer, 1993; Dubovik et al., 2000). The spectral fitting thus results in profiles of concentrations of species integrated along the LOS (slant profiles). The left panel of Fig. 1 gives an example of fits to transmission spectra at several altitudes obtained during a solar occultation, showing broad ozone absorption centered around 250 nm. CO_2 absorbs below 200 nm, but this part of the spectrum is very noisy in solar occultations and can only rarely be used for retrieving CO_2 density. Detection limit for the slant ozone column is $\sim 10^{19}$ m^{-2} (Lebonnois et al., 2006).

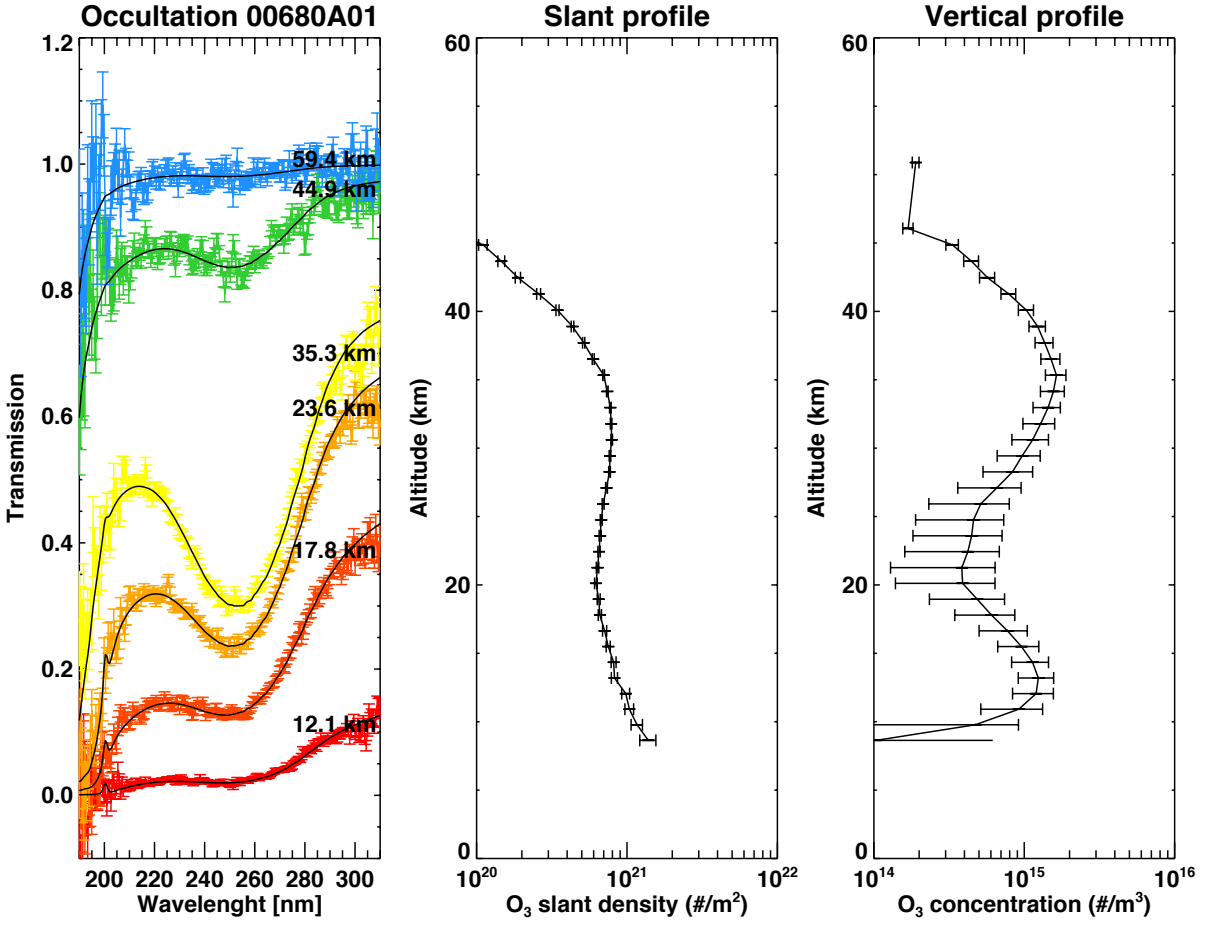

Figure 1: Left: An example of fits to transmission spectra from the solar occultation 680A01 (longitude: 77.2°E; latitude: 21.6°S; local time: 17.3; solar longitude: 68.0°). Colored solid lines: SPICAM/MEX UV transmission spectra as a function of wavelength. The color changes as a function of altitude, as indicated in the plot. Black solid lines: A fit of the model (Beer-Lambert law) to the transmission spectrum. Middle: The derived ozone slant density profile with error bars retrieved from the transmission spectra. Right: The ozone concentration profile with error bars obtained from the slant profile after vertical inversion.

The effect that aerosols have on the retrieval can be seen on the full wavelength range of the transmission spectrum in two ways: First, as a decrease in transmission with increasing optical thickness, and second, as a slope of the spectral continuum that depends on the particle size (see the left panel of Fig. 1, where the spectral slope is well visible in all of

the plotted transmissions). The aerosol extinction does not have a spectral signature correlated directly with the ozone absorption that is centered around 250 nm, thus, in theory, the effect of aerosols on the ozone retrieval is to reduce the transmission to such low values that it can be impossible to retrieve ozone absorption (in particular near the surface). However, in certain situations aerosol extinction combined with systematics led to detections of ozone that we now filter and qualify as false detections. We have eliminated these cases as described in the following section 2.3.

Because of telemetry constraints, only five "bands" of pixels can be transmitted for each acquisition out of the 288 lines of the CCD. These five "bands" have contiguous fields of view and are acquired by binning a predefined number of CCD lines. For stellar occultations, the central band receives the majority of the stellar light, the rest being spread over the four other bands. In solar occultation the large angular size of the Sun implies that every band receives light from a specific portion of the Sun. The binning is adjusted so as to download a nearly complete solar diameter. During solar occultation post-processing, we average the slant concentrations obtained from the five bands to construct a single slant profile of ozone, which also smooths the profile somewhat in the vertical dimension. The subsequent error assigned to each altitude corresponds to the standard error on the mean from the five bands. However, for solar occultations affected by a significant shift in the pointing, we might use less than five bands. Bands are rejected if the standard deviation of the median transmittance (expected to be 1) per observation between 90 and 200 km is above an empirical threshold of 0.01. Each slant concentration profile and its corresponding uncertainties are then passed to the vertical inversion routine.

For vertical inversion, we use the so-called onion-peeling method, which assumes that the atmosphere is spherically symmetric. Furthermore, the inversion is stabilized with the Tikhonov regularization. The vertical inversion routine then produces the local O_3 profiles. Detection limit for the slant ozone column (Lebonnois et al., 2006, 10^{19} m^{-2},) translates to values of the order of 10^7-10^8 cm^{-3} in local concentration. The vertical inversion leads to (inhomogeneous) modification of the measurement resolution (1-3 km) due to selection of input data (spectral fitting of transmissions may not always converge to positive values with well-defined error bars) and negative values in the results arising from the remaining oscillations of the solution due to insufficient stabilization of the vertical inversion method. The onion-peeling method does not account for the strong horizontal gradients around the terminator, but Piccialli et al. (2021) showed that this leads to a maximum error of 20% in the cases they studied.

2.3. Application of additional detection criteria

The O_3 slant uncertainties introduced in the previous paragraph and the derived signal-to-noise ratios (SNR[O_3] = O_3 slant column / error of O_3 slant column) are not sufficient to avoid spurious detections of O_3 that are actually non-detections (that we call false detections from now on). The standard inversion method described above led to frequent ozone detections at low and midlatitudes during the second half of the Martian year, where no ozone is expected to appear. When averaged, these detections could lead to ozone concentrations above 20 km similar to values encountered in the aphelion midaltitude ozone layer (of the order of 10^9 cm^{-3}), whereas the MGCM predicted values clearly below the SPICAM detection limit (Fig. 2). A careful inspection of the transmissions revealed that no clear ozone absorption was present in these cases, despite the claimed ozone detections by the inversion method. An in-depth study of these cases led us to adopt a quality check to filter out the false detections of ozone.

In this paper, we use the term "false detection" that encompasses the actual false positives that are due to apparent ozone signatures created by a combination of aerosol extinction and systematics and also the false negative cases where the detection is unconvincing and statistically does not differ from a non-detection.

We describe in the following the selection criteria used in the quality check to establish firm O_3 detections. The definition of the criteria is visualized in Fig. 3.

A visual inspection of the transmittance spectra revealed sometimes a mismatch between the strength of the O_3 spectral signature and the SNR[O_3]. This is for instance apparent in the spectrum (a) in Fig. 3 where the faint O_3 footprint in the spectrum is in stark contrast with a strong SNR[O_3] = 14.9. These problems might have a dual origin. First, the spectral fitting relies on the standard Levenberg-Marquardt method to minimize the χ^2 (Quémerais et al., 2006). This method is not immune to converging into local minima and therefore may lead to non-optimal fits for some observations. Second, the transmittance spectra are not free of systematics. Faint oscillations are visible in several spectra (also seen in Fig. 3). These might result from a change in the pointing during an occultation or from insufficient removal of dark current. Such oscillations can be caught by the [O_3] model, inflating artificially the retrieved slant O_3. This is what happens with the spectrum (b) in Fig. 3.

In order to avoid spurious detections of O_3 that arise from the problems described above, we introduce two additional criteria in addition to the SNR[O_3] to help establish the detection of the O_3 signature. It was a step-by-step

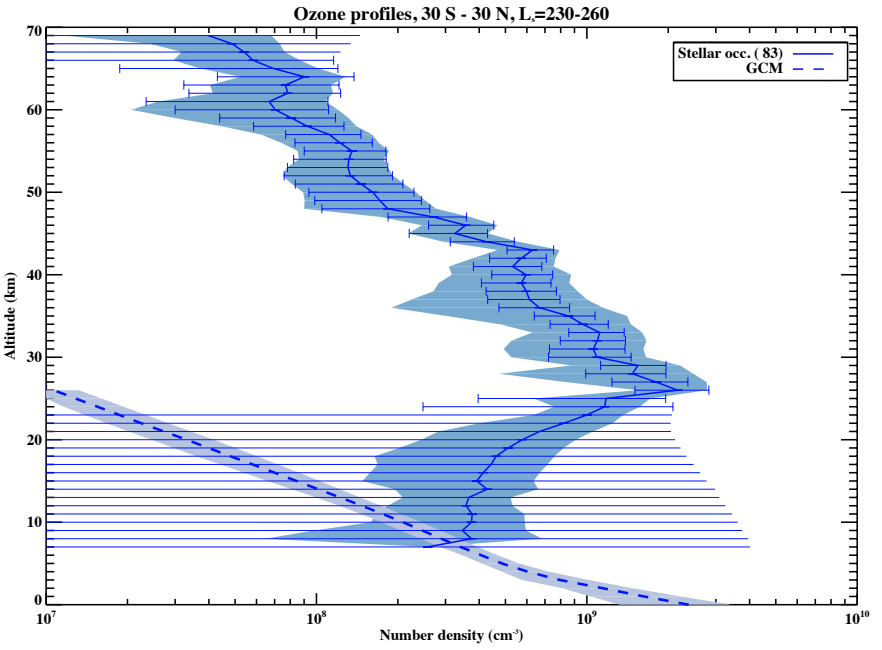

Figure 2: The unfiltered 2019 SPICAM stellar occultation dataset: Average profile of ozone (solid line, error bars, and 1-σ variability as the shaded area) around the perihelion (L_s=230-260° in the tropics (30°S-30°N). The average ozone profile from MGCM predictions is also plotted as the dashed line with the shaded area showing the 1-σ variability.

process to find the optimal criteria as we understood better and better the different sources of the false detections, and this lead to defining multiple criteria.

The first additional criterion is the ratio of the χ^2 of the [no O_3] model and the χ^2 of the [O_3] model (Ratio[O_3] = χ^2[no O_3] / χ^2[O_3]). This ratio is calculated in the wavelength range [210, 290] nm where the O_3 absorption is the strongest. So, for each spectrum, we perform the spectral fitting with two models : one with the slant O_3 as a free parameter [O_3] and the other one with O_3 fixed to zero [no O_3]. In some cases, the best fit or an equally good one is given by the second model ([no O_3]) even if the fit with the first model leads to a significant slant O_3. This criterion mainly eliminates bad fits due to convergence problems to a local minimum in the spectral fitting procedure. This criterion proved to be the most efficient filter for the false detections, pointing to the weakness of the Levenberg-Marquardt method being their main source.

These two criteria, SNR[O_3] and Ratio[O_3], are the natural statistical indicators to define if a signal is significant. Note that in the so-called maximum likelihood approach these two criteria are identical, which is however not the case here. Our method deviates from the maximum likelihood method as we use the ratio of the χ^2 of the fits, whereas the maximum likelihood relies on the difference of the χ^2 values.

The other additional, more empirical criterion is the Pearson's correlation coefficient in the wavelength range [210, 290] nm between the transmission spectrum and the [O_3] model, both corrected for the effect of aerosols. This has been done by subtracting the [no O_3] model from both. Thus, Correlation[O_3] is the correlation between (data – model[no O_3]) and (model[O_3]–model[no O_3]). In other words, if $Pe(X,Y)$ is the Pearson's correlation coefficient for X and Y, Correlation[O_3] = Pe(data – model[no O_3] , model[O_3]–model[no O_3]). This criterion was added to exclude O_3 detections spuriously produced by systematics or aerosols.

Our approach to excluding the false detections is iterative. We first reject O_3 detections from spectra with Ratio[O_3] < 1, thus where the fit is better without O_3 than with O_3. For the remaining observations, we use thresholds for the three criteria to determine if we have a detection. These criteria are used individually on each transmittance spectrum (instead of the full slant profile). If the three criteria, SNR[O_3], Ratio[O_3] and Correlation[O_3], are above their respective thresholds, we accept the O_3 value and call it detection. On the contrary, if at least one of the criteria is below its threshold, the O_3 value is not selected and is classified as an upper limit (see Fig. 3).

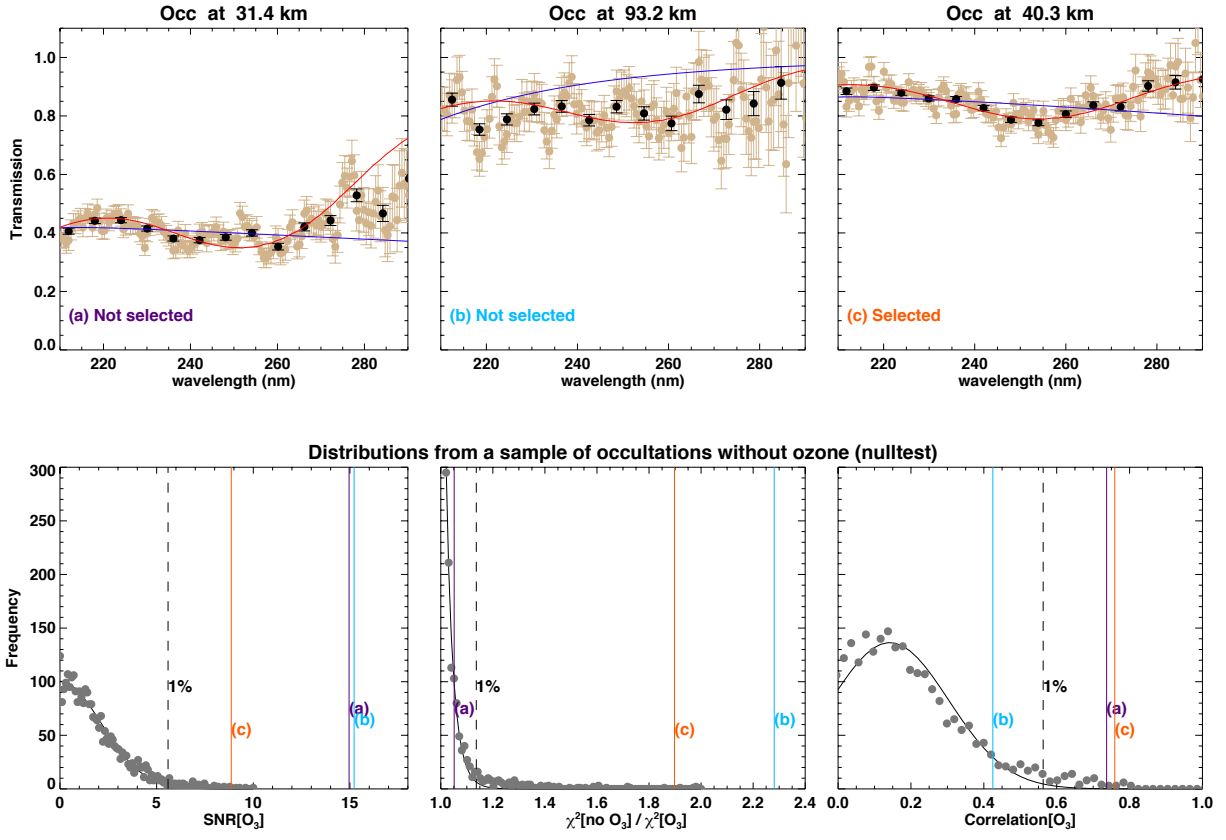

Figure 3: Top row: three examples (a-c) of SPICAM UV transmission spectra with the Beer-Lambert law fits (blue: without O_3; red: with O_3) from stellar occultations. The SPICAM spectra at full resolution are represented with light brown dots and error bars, while the black dots and error bars give the average SPICAM spectrum over 11 spectral points. Bottom row : the distributions (grey dots) for the three criteria from a null-test sample of stellar occultations with no O_3, and the fits to these distributions (continuous black lines). We consider O_3 is detected if the three criteria for a given spectrum are above the 1% threshold (dotted vertical lines). The colored vertical lines correspond to the cases in the top row: (a) purple lines, (b) blue lines, and (c) orange lines. Only spectrum (c) (orange vertical lines) fulfills the requirement of the three criteria above the 1% threshold, confirming ozone detection. Ozone is not detected in cases (a) and (b).

To compute the thresholds, we need to estimate the distribution of the three criteria for a null-test, i.e., for spectra that have no O_3 absorption. This null-test is defined separately for solar and stellar occultations. To build our null-test catalogues, we select two samples, one for stellar occultations, another for solar occultations. Both samples come from near the equator (latitudes 60°S-30°N) during the perihelion (L_s=240°-280°), thus at latitudes and season where and when the O_3 concentrations are very small. A visual inspection of the spectra from these samples confirms the lack of O_3. From the null-test set for stellar occultations, we derive the three distributions presented by grey dots in the three bottom plots in Fig. 3. We also derive the same distributions for solar occultations (not shown). To avoid the impact of outliers, we fit the distributions by Gaussian distributions (for SNR[O_3] and Correlation[O_3]) and a χ^2 distribution (for

Occultation	Ratio[O_3]	SNR[O_3]	Correlation[O_3]
Stellar: 1% (5%)	1.14 (1.08)	5.59 (4.25)	0.56 (0.46)
Solar: 1% (5%)	1.13 (1.08)	6.29 (4.79)	0.39 (0.33)

Table 1
Thresholds for the three different criteria as the limit for the upper 1% (and 5%) null-test population.

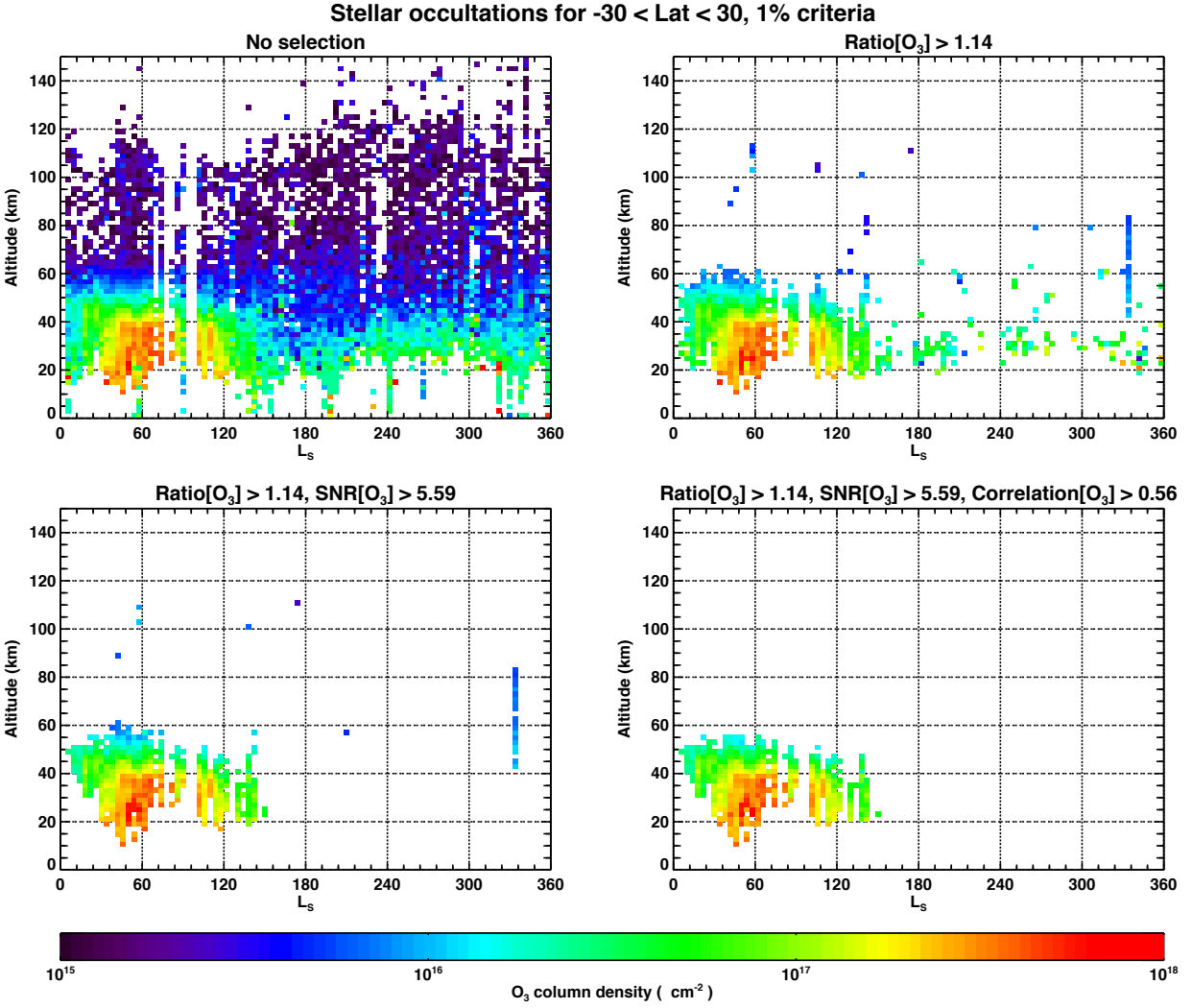

Figure 4: An example of the effect of the selection criteria on the ozone detections. Ozone column densities from stellar occultations in the tropics (30°S-30°N as a function of altitude and solar longitude. From upper left to lower right: No selection criteria used; Ratio[O_3] criterion; Ratio[O_3] and SNR[O_3] criteria; Ratio[O_3], SNR[O_3] and Correlation[O_3] criteria. The values of the thresholds are given in the figure titles and in Table 1.

Ratio[O_3]). From these fits, and separately for each criterion, we choose the thresholds as the limit of the upper-1% in the null-test populations for stellar and solar occultations independently. These thresholds are presented in Table 1.

Choosing the 1% threshold indicates that there is a 1% probability that a value above the threshold for a given criterion might be a false detection. The choice of the 1% threshold value is semi-empirical, resulting from balancing the number of false detections in the null-test sample and the number of detections in other samples. In practice, by

combining the three (only partially correlated) criteria, only 0.03% of the null-test observations give a false detection for stellar occultations and 0.13% for solar occultations. The effect of the three criteria can be seen in Fig. 4: the Ratio[O_3] criterion removes the vast majority of the false detections at all altitude ranges, SNR[O_3] removes a large amount in lower altitudes, and the final criterion, Correlation[O_3], discards the final spurios detections especially at higher altitudes.

Two additional thresholds, not presented in Fig. 3, corresponding to a limit at 5% and at 10% define respectively populations of spurious and very spurious detections. These two populations are very small and are eventually classified as upper limits. The 5% detection population could be identified as a "grey zone" where there are potentially real ozone detections that have been discarded by the very conservative 1% limit. However, including the small 5% detection population does not change the overall results. The 5% threshold values for the three criteria are also given in Table 1, for reference.

There are 83, 571 spectra from stellar occultations and 33, 506 from solar occultations between 0 and 80 km with retrievals. Out of these retrievals, only 6380 (7.6%) from stellar occultations and 3916 (11.7%) from solar occultations satisfied the three criteria of O_3 detection and therefore are selected. This selection is done for the O_3 slant densities after the spectral fitting and before the vertical inversion. Thus, only 10, 296 selected slant densities were then vertically inverted.

Naturally, the choice of the null-test sample is subjective and affects the values of the thresholds. Our visual inspection aimed at guaranteeing that the null-test sample is dominated by spectra that have no ozone signature, but some presence of ozone can not be excluded. Although their presence does not have a large effect on the values of the thresholds, this might lead to discarding some real ozone detections.

2.4. Observational coverage

The observational coverage of all analyzed solar and stellar UV occultations is presented in Figure 5. The overall combined latitudinal coverage of both occultation types is good, but depends strongly on the season (top panel of Fig. 5). Solar occultations do not probe well the equatorial regions nor the winter poles, whereas the latter are well covered (at least in the south) by stellar occultations. The latitude-longitude coverage (second panel of Fig. 5) is rather dense overall when accounting for both occultation types. One may note the scarcity of stellar occultations at high northern latitudes. The local times are (mainly) limited to nighttime (stellar occultations) and sunrise/sunset (solar occultations), creating a particular pattern seen in the third panel of Fig. 5. At high latitudes, solar occultations can be acquired at all local times (all seasons taken together), but at low latitudes sunrise and sunset occurs, respectively, around 6 AM and 6 PM. Stellar occultations are acquired during nighttime at all latitudes, but those taken at high latitudes during the polar night can be recorded at any local time (as can be seen in the southern hemisphere, third panel of Fig. 5). The bottom panel of Fig. 5 shows the occultation coverage as a function of orbit number and Mars Year. The largest gaps in the coverage are in low latitudes for solar occultations and at high northern latitudes for stellar occultations.

As described in Section 2.3, we applied strict criteria on the fits, eliminating a fair amount of false ozone detections. The colored symbols in Figure 5 show the occultations in which ozone was detected after application of these criteria. The detections concentrate in the first half of the Martian year whereas the second, dustier half is void of ozone detections.

2.5. The LMD Mars Global Climate Model

To interpret the SPICAM ozone measurements we have used the LMD Mars General Circulation Model (MGCM, Forget et al., 1999) with photochemistry initially described by Lefèvre et al. (2004). The version used here includes all the recent improvements of the physics of the LMD MGCM, such as the radiative impact of water ice clouds (Madeleine et al., 2012) as well as the improved cloud microphysics and water cycle (Navarro et al., 2014). Regarding the photochemistry, we have implemented the semi-implicit method described by Cariolle et al. (2017) to solve the system of chemical equations associated with the evolution of the species concentration. The photochemical and kinetics data have been updated to the latest compilation in use for atmospheric studies (Burkholder et al., 2015), and heterogeneous chemistry is included as in Lefèvre et al. (2021). In the configuration used here, the model was integrated with a horizontal resolution of 5.6° in longitude and 3.75° in latitude on 73 levels from the surface up to 200-300 km, and the outputs are done every 15 minutes. The frequent outputs allow acquisition of model profiles without time interpolation as close to the local time of the observations as possible, which is important particularly in the case of solar occultations. The used model dust scenario (Montabone et al., 2015) is the one for MY 27, which represents a typical MY during the SPICAM UV dataset (MYs 27-31, excluding MY 28). In the first half of the year

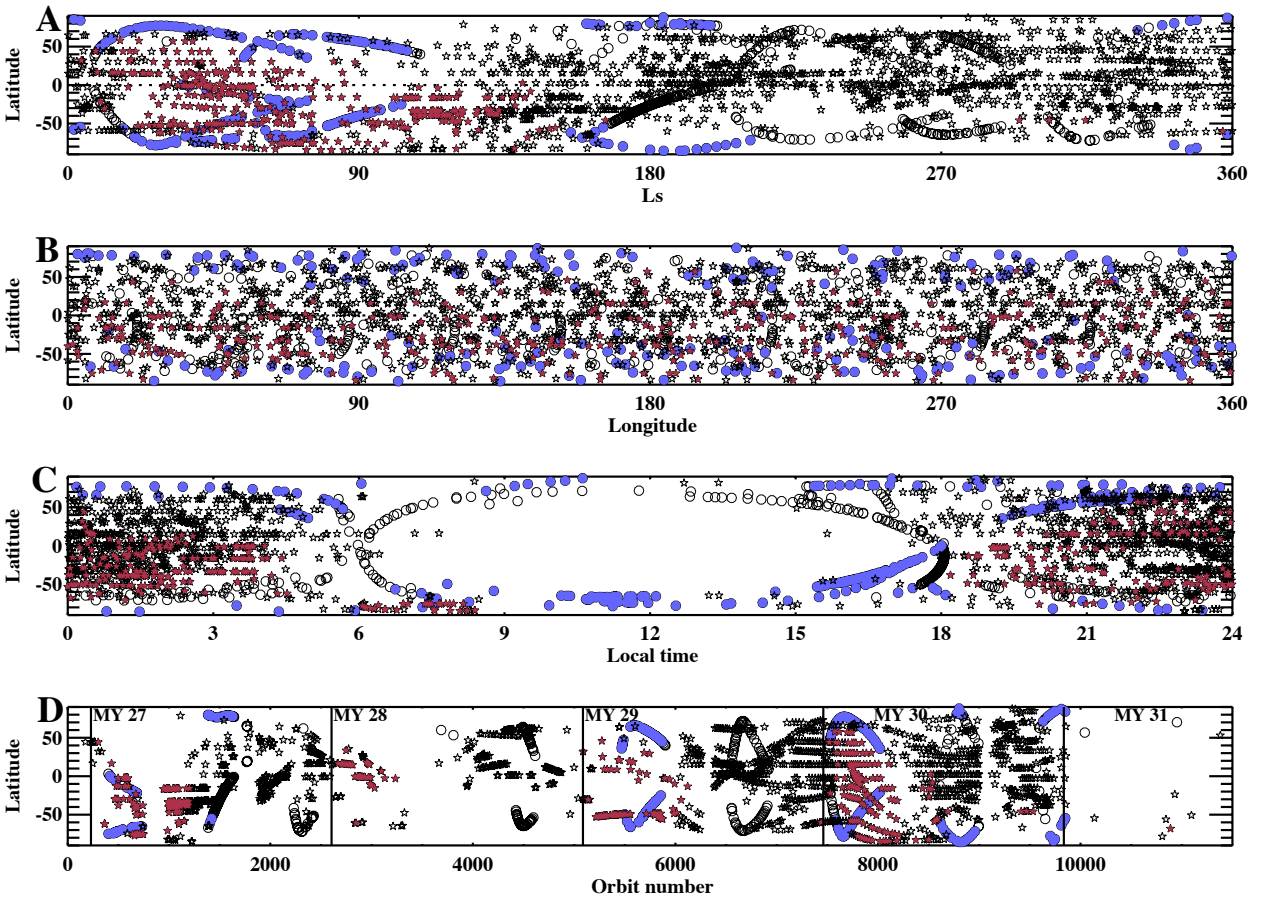

Figure 5: Coverage of SPICAM/MEX UV channel occultations. Circles: solar occultations. Stars: stellar occultations. Blue circles and red stars indicate the occultations in which ozone was detected in this study using the criteria described in Section 2.3. The distribution of the occultations is given as a function of: A: latitude and solar longitude; B: latitude and longitude; C: latitude and local time; D: orbit number (with Mars Years as noted in the figure and separated with vertical lines).

(L_s=0-180°) there is very little interannual dust variability among the MYs 27 to 30, and thus ozone modeling is not biased by the chosen scenario. The second half of the year (L_s=180-360°) does not display interannual variability in the modeled ozone abundances because ozone is close to zero in all years. The solar flux chosen is constant, but solar variability has little effect on Martian ozone.

3. Results

In the following we present the overall climatology of ozone vertical distribution on Mars acquired from SPICAM UV occultations and a first-order comparison to the MGCM-modeled ozone vertical distribution. Then a focused discussion is provided for a number of interesting cases.

3.1. Seasonal distribution of ozone

The figures presented in the following show binned and averaged profiles as decribed below. We are not including here figures on the observational uncertainties since they would be hard to interpret in this type of plots, but the interested reader is invited to explore the individual profiles and their error bars by accessing them in the data repository indicated in the Data availability section. The LMD MGCM profiles, whose local time differs by at most 7.5 minutes from the observation time thanks to the short model output timestep of 15 minutes, have been interpolated from the nearest model grid points to the latitude and longitude coordinates of the observation and then averaged in a grid of

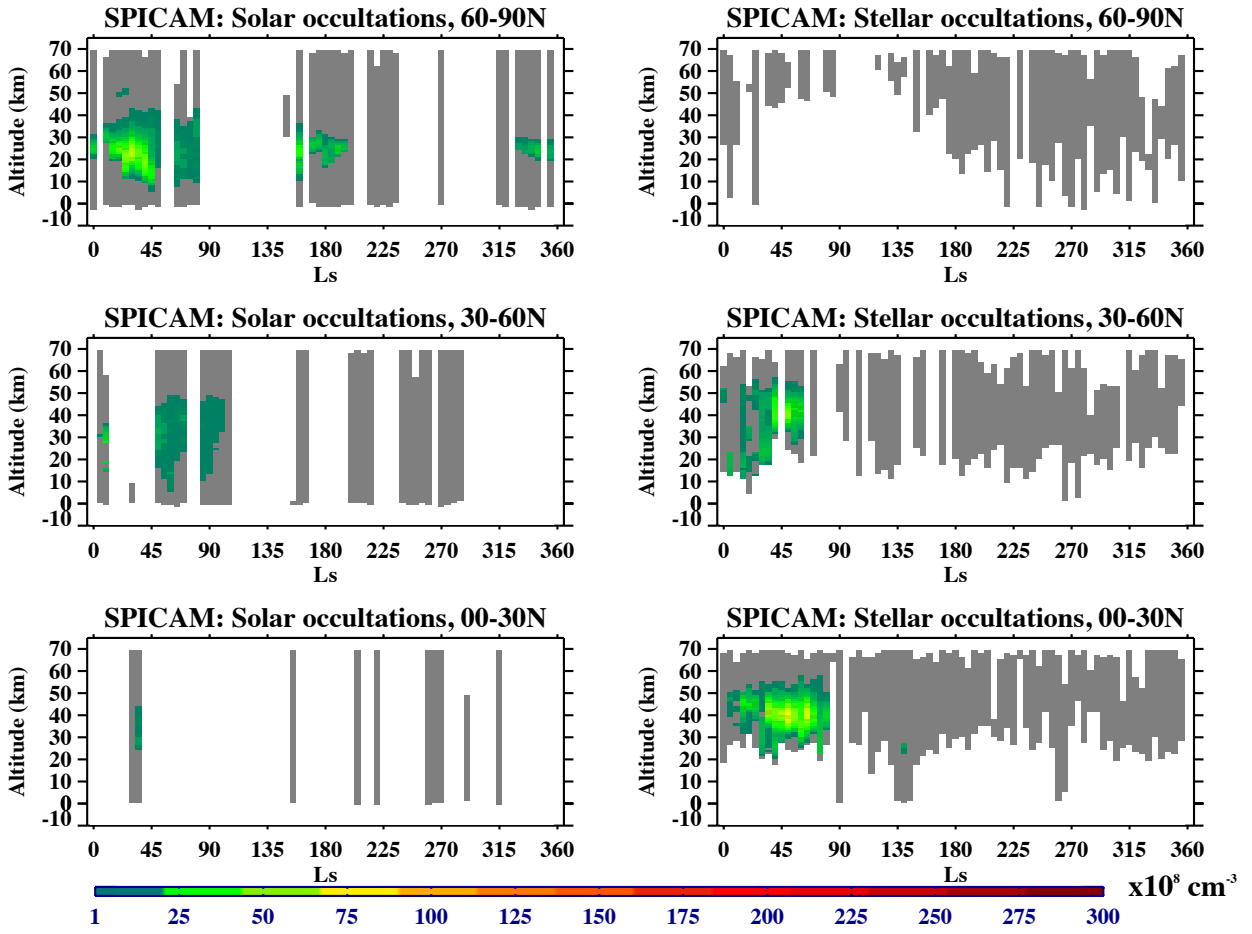

Figure 6: Ozone concentrations as measured by SPICAM as a function of altitude above the areoid and solar longitude for three latitudinal bands in the northern hemisphere, binned and averaged in a grid of 1 kmx5° L_s. Left: solar occultations. Right: stellar occultations. The color scale goes from 1 to 300·10^8 cm^{-3} (all values above 300 · 10^8 cm^{-3} are assigned the same deep red color). White areas indicate where there were no observational data and grey areas are the ones with data but no confirmed O_3 detection.

5° in solar longitude. The observed profiles have been first interpolated in vertical grid of 1 km altitude resolution, corresponding to the model output vertical grid, and then averaged in a grid of 5° in solar longitude. The grey zones in the SPICAM figures represent zones where SPICAM observations exist, but the spectral fit to the data failed or was rejected (see section 2.3 describing the selection criteria). It can be seen that our strict selection criteria eliminate a large part of the observations, where O_3 detections are not statistically confirmed. The remaining profiles provide the fully validated O_3 dataset from SPICAM UV occultations.

3.1.1. Northern hemisphere

Figures 6 and 7 show, respectively, the observed and modeled ozone vertical distributions in the northern hemisphere for different latitude zones and as a function of solar longitude, combining all observations from different Martian Years.

Overall, the general features of Martian ozone (e.g., aphelion ozone layer, large concentrations in the lower atmosphere) are visible in the model results, whereas the observations are mainly able to probe the mid-altitude ozone layers in low and midlatitudes and at the poles. SPICAM detects some ozone below 10-15 km, so it could in principle see the O_3 concentration increasing towards the surface in the near-surface layer; however, the statistics are poor since no confirmed ozone detections were acquired at the very lowest altitudes. There are several qualitative and quantitative differences that will be reported in more detail below.

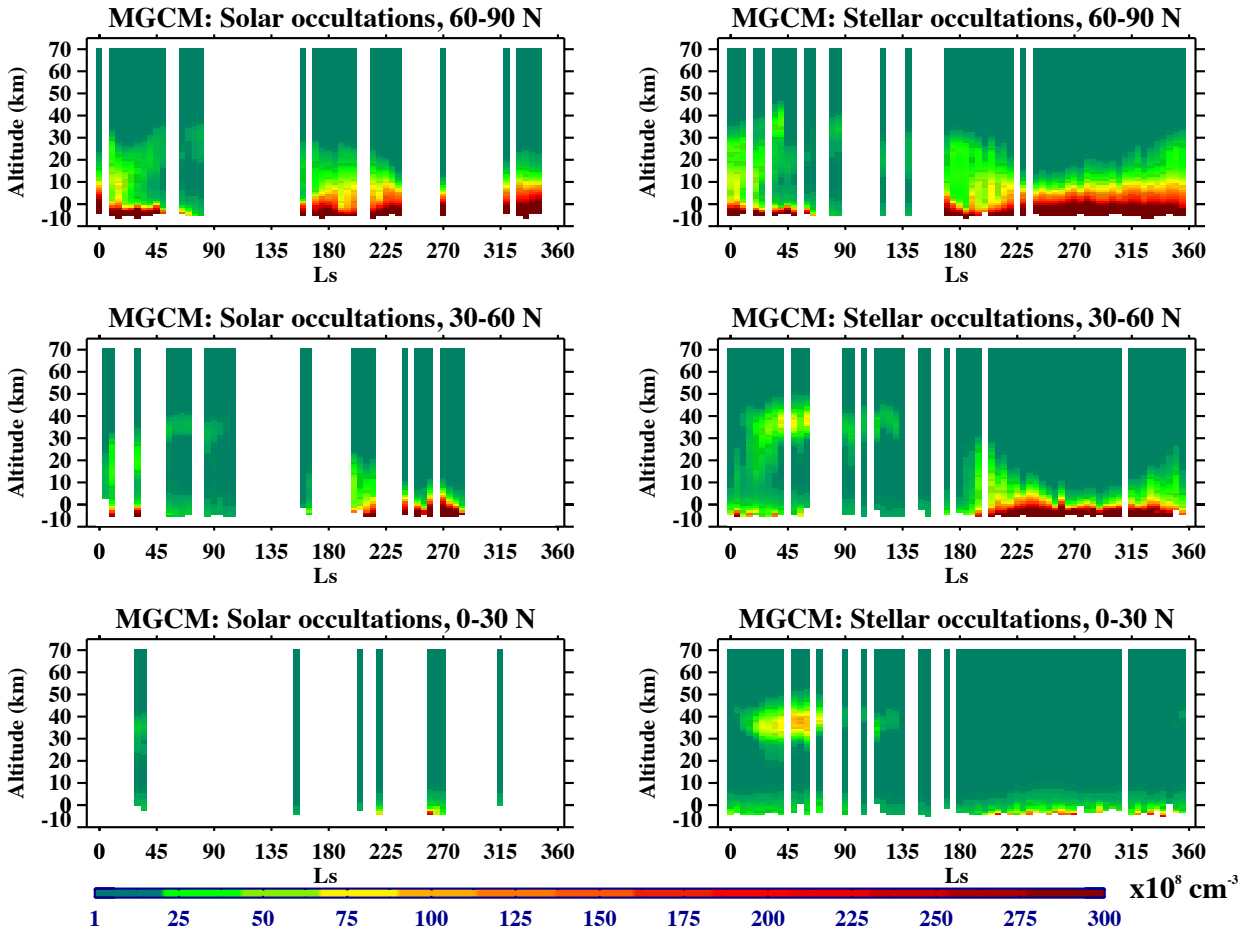

Figure 7: LMD MGCM-modeled ozone concentrations as a function of altitude above the areoid and solar longitude for three latitudinal bands in the northern hemisphere corresponding to solar (left) and stellar (right) occultations of SPICAM,, binned and averaged in a grid of 1 kmx5° L_s. The color scale goes from 1 to $300{\cdot}10^8$ cm^{-3} (all values above $300 \cdot 10^8$ cm^{-3} are assigned the same deep red color). White areas indicate where there were no observational data.

In the low to mid northern latitudes probed by stellar occultations, the nocturnal ozone layer observed around 40 km between L_s=30-90° is overall well reproduced by the LMD MGCM. This so-called aphelion ozone layer will be discussed in more detail in Section 3.2.1.

In high northern latitudes in the spring (L_s=10-90°), solar occultations reveal the ozone layer between 10 and 40 km. This is discussed further in Section 3.3.2.

3.1.2. Southern hemisphere

Figures 8 and 9 show, respectively, the observed and modeled ozone vertical distributions in the southern hemisphere.

As mentioned already for the northern hemisphere, one of the salient features of the low and midlatitude ozone distributions (0-30°S and 30-60°S) in the aphelion season is the mid-altitude ozone layer, seen very well in stellar occultations in the range L_s=30-120°, and it can also be seen in solar occultations. The aphelion layer is very well reproduced by the LMD MGCM, with peak concentrations and altitudes matching nearly everywhere during the night, and quite well also at terminators. These aspects will be discussed more in detail in Section 3.2.1.

In the first half of the Martian year, in midlatitudes (30-60°S), a hint of the top of the near-surface layer is seen (local ozone maximum around 10-20 km from L_s=40-100°).

In high southern latitudes in the polar winter SPICAM measurements and the model predictions are in fair agreement. Our profiles also contain evidence of the polar mid-altitude ozone layer around 50 km (Montmessin and Lefèvre,

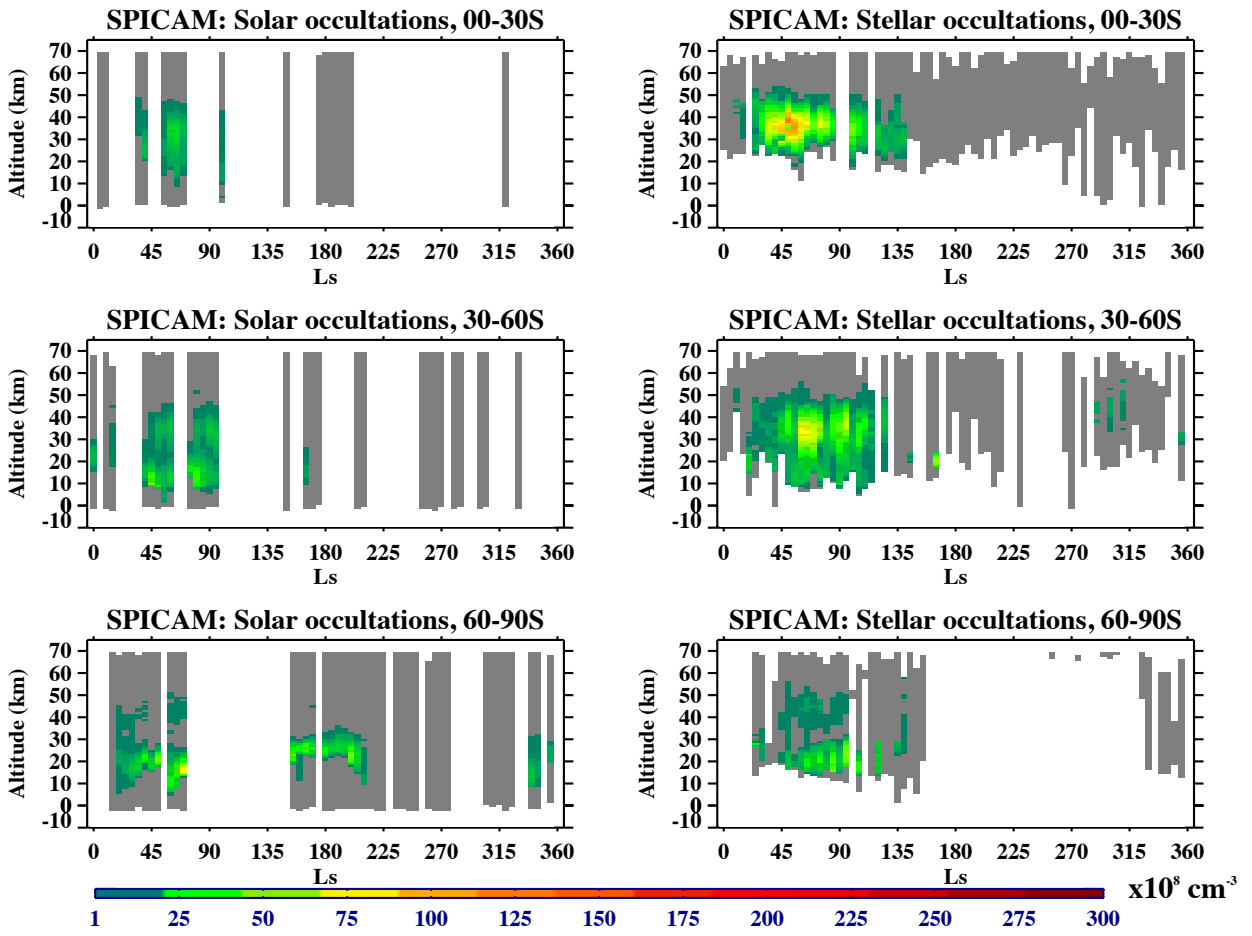

Figure 8: Ozone concentrations as measured by SPICAM as a function of altitude above the areoid and solar longitude for three latitudinal bands in the southern hemisphere, binned and averaged in a grid of 1 kmx5° L_s. Left: solar occultations. Right: stellar occultations. The color scale goes from 1 to 300·10^8 cm^{-3} (all values above 300 · 10^8 cm^{-3} are assigned the same deep red color). White areas indicate where there were no observational data and grey areas are the ones with data but no confirmed O_3 detection.

2013). These features will be discussed in Section 3.3.1.

3.2. Focus on low and midlatitudes

3.2.1. Northern spring and summer

In the aphelion season, the atmosphere is cold due to the large distance of Mars from the Sun and to the low dust optical thickness. This leads to a low hygropause (water condensation level) and a very dry middle atmosphere. Consequently, relatively high ozone concentrations can be produced above the hygropause. A distinct feature of the ozone vertical distribution is a nocturnal layer of ozone above the hygropause, around 30-40 km, during the aphelion season. The increase in water vapor concentrations and the progressive rise of the hygropause leads to the disappearance of this layer later in the summer, after L_s=100° in solar occultations (no data) and prevailing until L_s=130° in stellar occultations. This ozone layer and its diurnal and seasonal variations are predicted by modeling and have been previously reported from stellar occultations (Lefèvre et al., 2004; Lebonnois et al., 2006; Gröller et al., 2018) and solar occultations (Khayat et al., 2021; Patel et al., 2021b).

The mid-level aphelion ozone layer observed with SPICAM occultations and modeled with the LMD MGCM can be seen in Figs. 6, 7, 8 and 9. The layer is easily discernible in occultations at all latitudes from 60°S to 60°N, with the highest concentrations observed in the latitude range 0-30°S. This is in line with O_3 nadir measurements (Perrier et al., 2006; Clancy et al., 2016) that also indicate larger O_3 column values in the Southern hemisphere (0-30°S versus

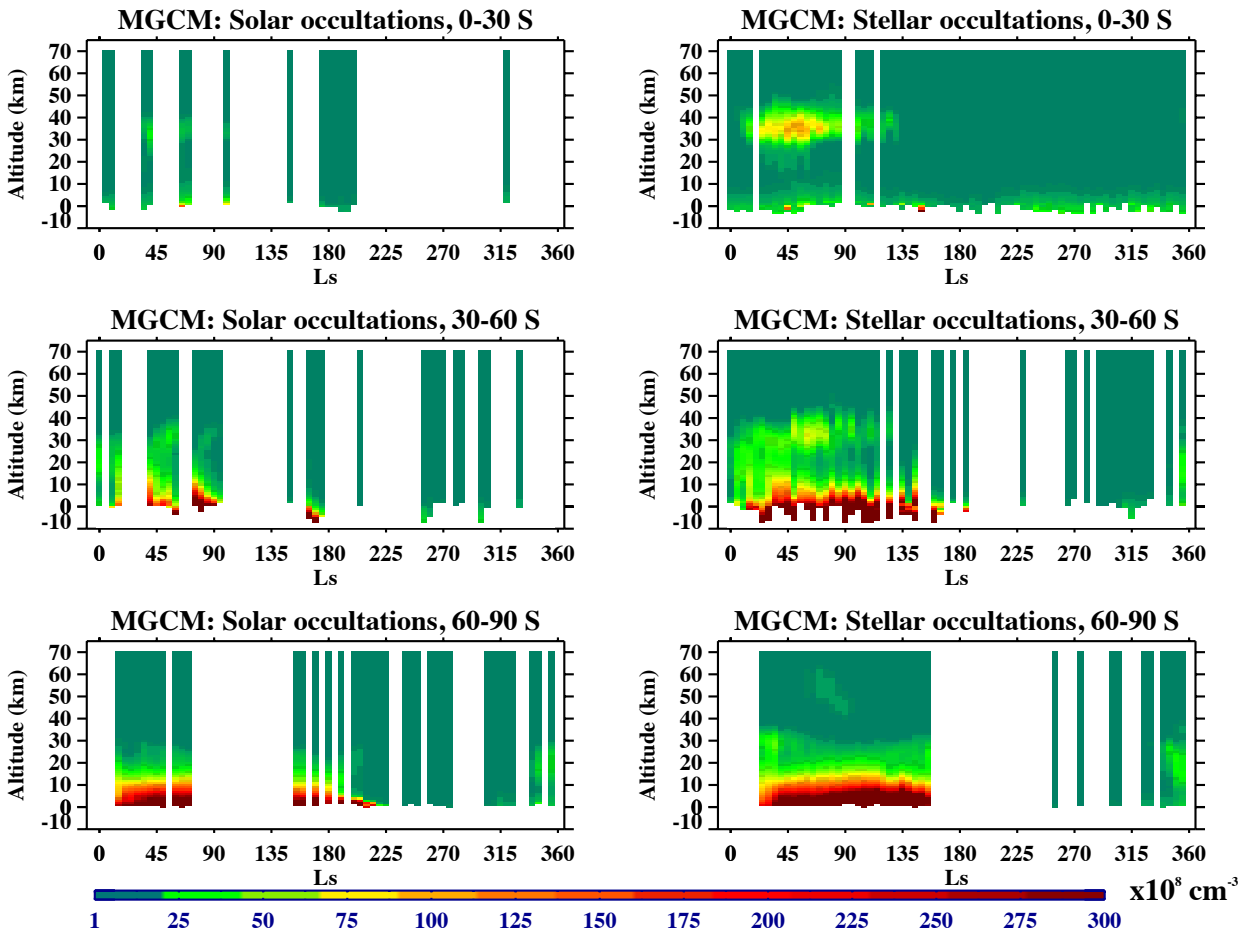

Figure 9: LMD MGCM-modeled ozone concentrations as a function of altitude above the areoid and solar longitude for three latitudinal bands in the southern hemisphere corresponding to solar (left) and stellar (right) occultations by SPICAM, binned and averaged in a grid of 1 kmx5° L_s. The color scale goes from 1 to 300 · 10^8 cm^{-3} (all values above 300·10^8 cm^{-3} are assigned the same deep red color). White areas indicate where there were no observational data.

0-30°N). On the contrary, this asymmetry is not predicted by the model that indicates very similar ozone distributions above 20 km in the tropical latitude ranges on both hemispheres (0-30°S and 0-30°N).

We will compare averaged profiles from both occultations and model results. Fig. 10 shows, in 12 panels corresponding to the four concerned latitude bands of 30 degrees and for three L_s ranges, the averaged vertical distribution of ozone. When both solar (blue lines) and stellar occultations (red lines) are available, we can track a part of the diurnal cycle (day-night transition) of the ozone layer. The average profiles show how the ozone concentration in the layer is larger during the night, as expected, due to the absence of photolysis. At the terminator, corresponding to solar occultations, ozone photolysis leads to significant ozone decrease. Qualitatively and quantitatively, the ozone layer behavior is very similar in SPICAM observations and in the MGCM.

The two top rows of Figure 10 show the average profiles of ozone for the northern hemisphere midlatitudes (30-60°N) and low latitudes (0-30°N). Comparing the model to the observations in the nighttime (stellar occultation) ozone profiles, the ozone concentrations seem to be peaking at slightly higher altitude in the model, except for the midlatitude profile at L_s=60-90° (first row, middle panel). The observed maximum concentrations are lower than the modeled ones by a factor of two, except for the nearly perfect correspondence for stellar occultations at L_s=60-90° in the midlatitudes (red curves: first row, middle panel). The solar occultations have dense data coverage in 30-60°N during the whole seasonal range (L_s=30-110°), but the observed ozone concentrations are below the modeled ones and do not have a prominent peak (red lines in all three panels in the first row).

The two bottom rows of Figure 10 show the average profiles for low (0-30°S) and mid (30-60°S) southern latitudes

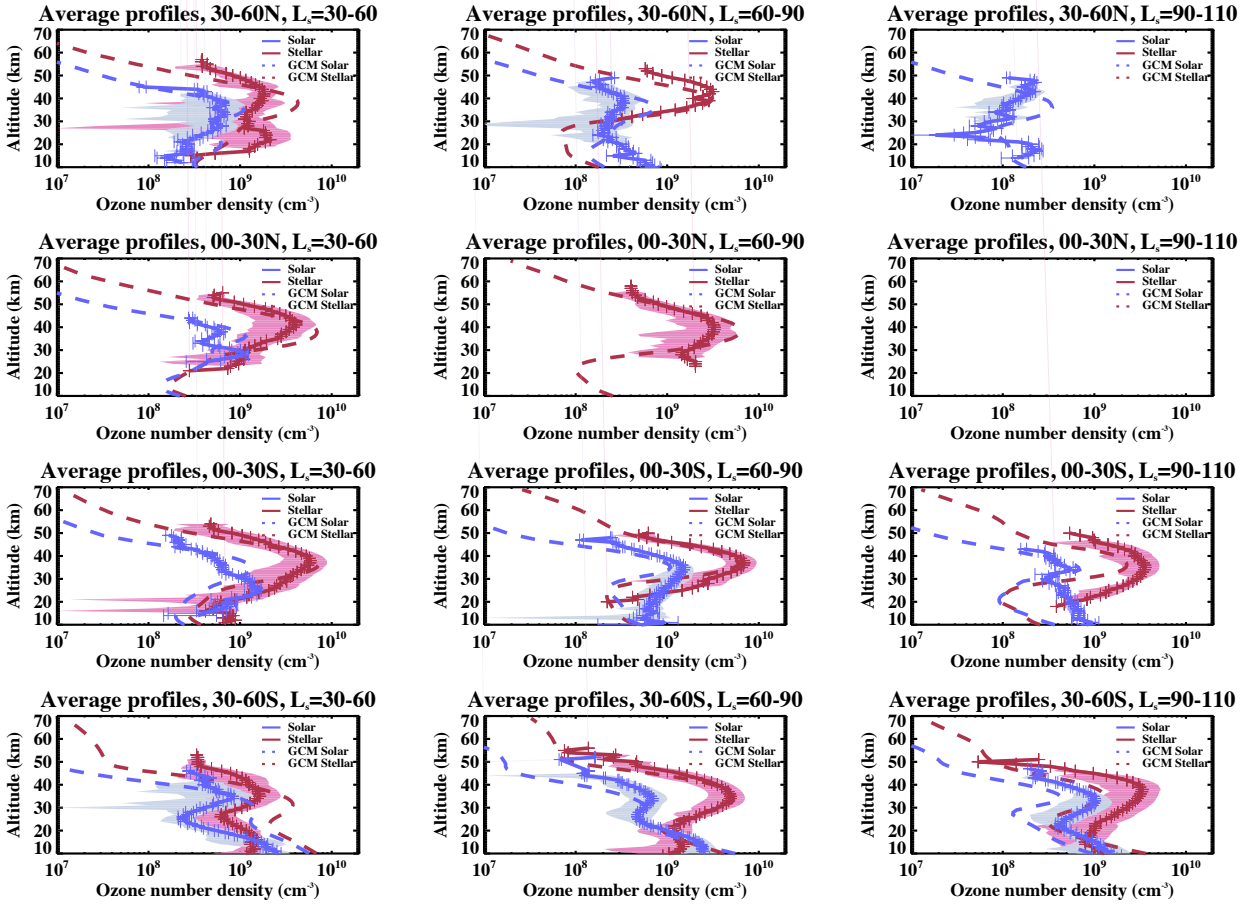

Figure 10: Average ozone concentration profiles (cm^{-3}) as a function of altitude above the areoid for four low-to-midlatitude bands in three L_s intervals at the Northern spring, as marked in the figure. SPICAM occultations (stellar: red; solar: blue) are shown with solid lines with error bars giving the uncertainties of the average and colored zone showing the 1-sigma dispersion of the averaged profiles. MGCM average profiles are shown with dashed lines. The 1-sigma dispersions are only calculated for altitudes where at least two data points were available.

for the range of L_S=30-110°. Here the observational statistics are quite good with data from both occultation types. Overall, the observed and modeled nighttime ozone concentrations are higher than at the terminator, as expected. The MGCM captures well the behavior of the ozone layer above 30 km, but in some cases there are quantitative differences.

In the Southern low latitudes (0-30°S) in L_S=90-110° (rightmost panel, third row), the O_3 layer seen by SPICAM stellar occultations (red) is a factor of two higher than the modeled one between 20-50 km, while abundances seen by solar occultations (blue) are a factor of several higher than the model below 30 km. This could point towards the real atmosphere being drier and having a lower hygropause than in the model. In these low Southern latitudes, a very prominent terminator peak is observed (and well modeled) in L_S=60-90° (middle panel, third row) with concentrations lower by a factor of six compared to the nighttime peak.

At latitudes 30-60°S, both the nighttime and the terminator ozone layers are observed about 5 km higher than predicted by the model at L_S=30-60° (left panel, fourth row), but the peak altitudes are very well reproduced by the

model during the other time intervals (middle and right panel, fourth row). In these latitudes (fourth row), the observed nighttime ozone peak concentrations (red) are lower than modeled concentrations in L_s=30-60° (left panel), similar in L_s=60-90° (middle panel) and higher in L_s=90-110° (right panel). The terminator ozone peak (blue) at these Southern midlatitudes (fourth row) is well defined in altitude, but is observed slightly higher than the modeled one (left and middle panels), except in L_s=90-110° (right panel). The peak concentration values at the terminator (fourth row, blue) are lower in L_s=30-60° (left panel), similar in L_s=60-90° (middle panel), and higher by a factor of two in L_s=90-110° (right panel).

Clancy et al. (2017) found that above 50 km at these latitudes the MGCM underestimated the $O_2(^1\Delta_g)$ dayglow (that is chemically correlated with ozone) compared to CRISM data and they related this to problems in modeling the water cycle, leading to too much water vapor in certain seasons and zones. Unfortunately we do not have data points above 50 km in the filtered dataset and can not perform an extensive comparison, but there are hints of an underestimation by the model around 50 km.

Although IUVS (Gröller et al., 2018) measured maximum nighttime ozone concentrations in the aphelion layer in mid and low latitudes that were a factor of five smaller than concentrations measured by SPICAM by Lebonnois et al. (2006), it should be noted that the ozone layer shows variability (see the shaded regions in the figures) and that our average peak concentration ($3{\cdot}10^9$) and its variability at 0-30°N in L_s=60-90° are in good agreement with the values of IUVS (Figure 15c of Gröller et al., 2018). IUVS also observes the gradual disappearance of the layer after northern hemisphere summer solstice, confirmed by our work and already reported by Lebonnois et al. (2006). It should be kept in mind that IUVS and SPICAM did not observe during the same Mars Years.

3.3. Focus on high latitudes

3.3.1. High southern latitudes (60-90°S), southern fall/winter (L_s=0-100°)

A mid-altitude ozone layer was detected in the Southern polar night with SPICAM stellar occultations by Lebonnois et al. (2006), and the formation of this layer was explained by Montmessin and Lefèvre (2013) through the analysis of a larger sample of SPICAM/MEX UV stellar occultations. Recently, this ozone layer was also probed by the NOMAD (Nadir and Occultation for MArs Discovery) instrument on ExoMars Trace Gas Orbiter (Khayat et al., 2021; Patel et al., 2021b), and we make a comparison with their profiles in Section 3.4.

The Southern polar night ozone profiles present a two-layer structure. The mid-altitude ozone layer around 50 km is a result of poleward, downwelling transport of oxygen atoms into the polar night from lower latitudes by the Hadley circulation (Montmessin and Lefèvre, 2013). The near-surface layer results from the absence of photolysis and the extreme dryness of the very cold Southern polar vortex, allowing high ozone concentrations throughout the winter.

In this paper we have an opportunity to combine SPICAM solar occultations with the full stellar occultation dataset to study the midaltitude ozone layer within and at the edges of the Southern polar night. Note that the solar occultations follow the edge of the polar night (the terminator) whereas the stellar occultations can probe the interior of the zone. We compare the SPICAM observations with the MGCM results for the ozone concentrations in the averaged profiles (Fig. 11) in different latitude-season ranges.

Going through the ozone profile development as a function of season (Fig. 11), it can be seen that the fairly high ozone concentrations (10^8-10^9 cm^{-3}) are observed between 40 and 50 km already in the first part of the polar night, both during night and at its edge, at L_s=40-60° (top left panel of Fig. 11). The model does not, however, predict such high values at this season, although there is a hint of a layer or high values at a similar altitudes but with an order of magnitude difference. This suggests that the mean meridional circulation, downwelling above the pole and transporting the oxygen atoms necessary for the formation of this layer, is too weak in the MGCM during this period. Such a result is consistent with the lack of $O_2(^1\Delta_g)$ nightglow in the MGCM with respect to CRISM retrievals over the South pole at $L_s = 50°$ (Clancy et al., 2013). In the following L_s ranges, the O_3 high-altitude layer seems to be peaking just below 50 km. However, as there are very few SPICAM detections above 50 km, the layer structure and actual peak altitude can not be defined well. The maximum concentrations observed are around $6\text{-}7{\cdot}10^8$ cm^{-3} in stellar occultations and $2\text{-}3{\cdot}10^8$ cm^{-3} in solar occultations. The peak concentrations for stellar occultations are similar in the model, but the modeled peak is centered closer to 55-60 km, about 10 km higher than the detected one. The model does not predict a terminator ozone peak that would have values above 10^7 cm^{-3}. This points towards the model downwelling circulation being too constrained over the pole and lasting during too short a period during the winter. Moving to the end of the studied period, the model is in good agreement with the scarce stellar occultation detections in L_s=80-100° with a peak around 45 km with concentrations of $3\text{-}4{\cdot}10^8$ cm^{-3}.

In the lower atmosphere, at 15-25 km altitudes, the observed concentrations are slightly higher than in the MGCM.

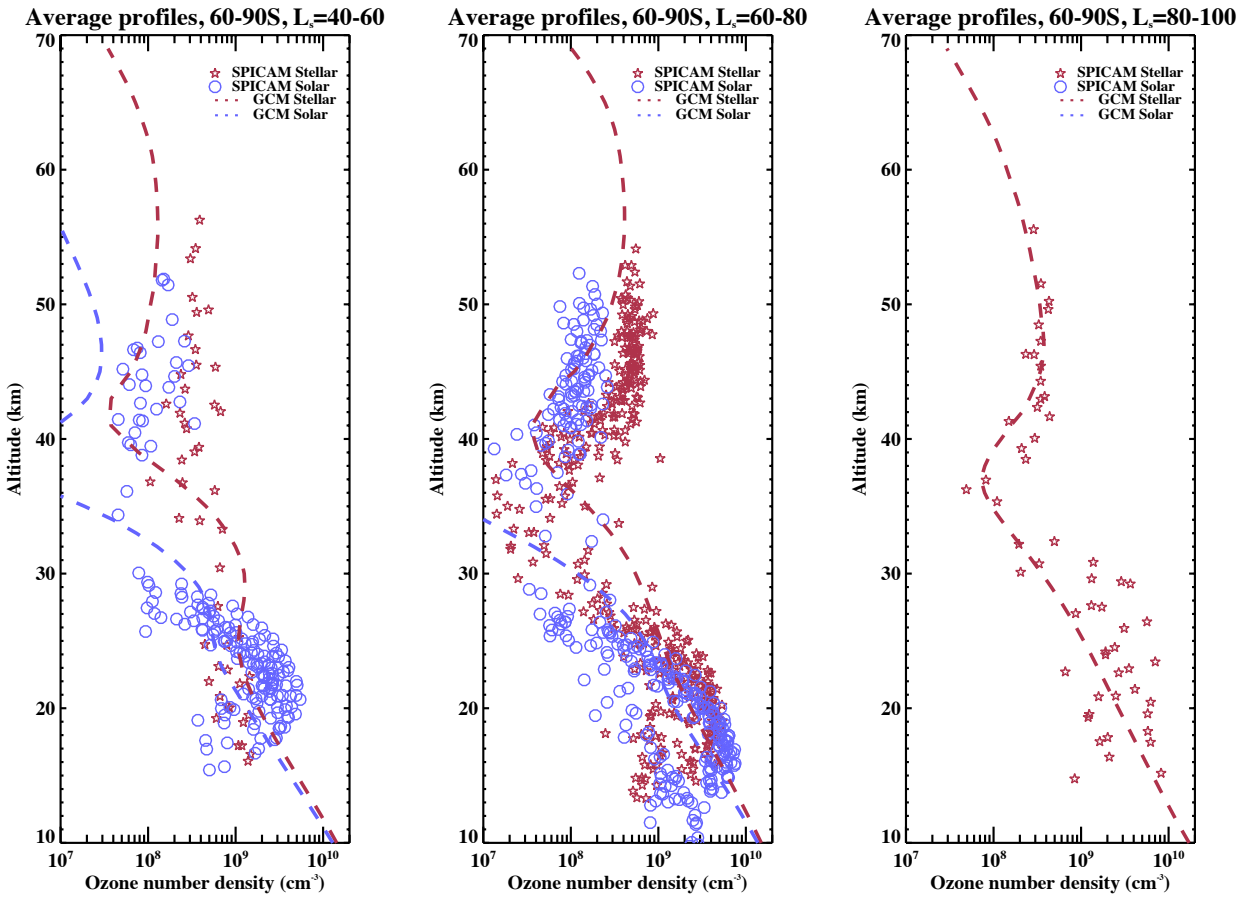

Figure 11: All individual SPICAM ozone concentration measurements (cm^{-3}) as a function of altitude above the areoid for Southern high latitudes (60-90°S) in three L_s intervals at the Northern spring (L_s=40-100°), as marked in the figure. SPICAM occultations (stellar: red stars; solar: blue circles). MGCM average profiles are shown with dashed lines.

There also seems to be a 5-10 km shift in altitude of the profiles in L_s=40-60° and L_s=60-80°: the modeled minimum between the ozone layers is found at a higher altitude than the observed one. In addition, there is a local enhancement of ozone concentrations in the model between 25-35 km: this might correspond to a similar behavior seen in SPICAM measurements between 15 and 25 km. The model also underestimates the ozone concentrations between 20 and 30 km at L_s=80-100°. However, the shape of the SPICAM profile bringing out the enhanced concentrations may also be related to an artefact of decreasing ozone concentrations in the lower end of the profile caused by the vertical inversion routine. In any case, the apparent shift in altitude of otherwise similarly behaving profiles calls for a more detailed investigation of the model ozone.

3.3.2. High northern latitudes (60-90°N)

Although there are some stellar occultations in the high northern latitudes, no ozone detections were acquired. We can look into the behavior of O_3 in this region with solar occultations.

Left and middle panels of Figure 12 show the SPICAM O_3 vertical distribution averaged over 60-90°N for the periods L_s=10-60° and L_s=60-90°. SPICAM detects the O_3 winter-spring polar layer forming in the lowest atmosphere. The model underpredicts the ozone concentrations above 15 km in L_s=10-60° but is close to observations in L_s=60-90°. The underestimation of ozone by the model in early spring is consistent with the too low ozone columns calculated by the LMD MGCM with respect to the SPICAM observations in nadir mode (Lefèvre et al., 2021). The present ozone deficit could be attributed to an overestimation of the water vapor (i.e., wet bias) above 15 km. Alternatively, it could be due to the too efficient HO_x-catalyzed ozone loss obtained with current gas-phase kinetics data on Mars (Lefèvre et al., 2021). The detailed study of such processes is beyond the scope of the present publication and

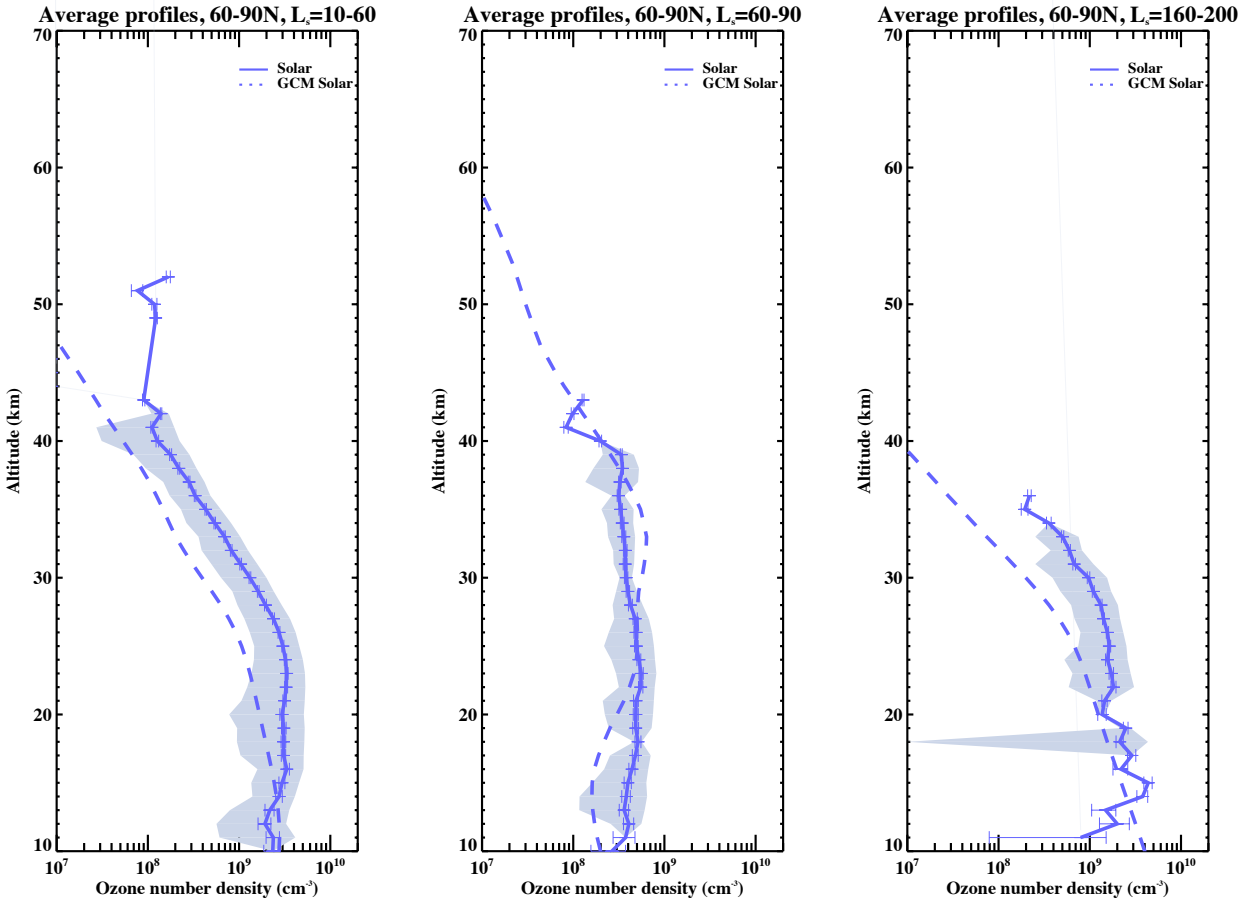

Figure 12: Average O_3 concentration (cm^{-3}) as a function of altitude above the areoid (km) at high northern latitudes (60-90°N), in spring (left: L_s=10-60°, right: L_s=60-90°) from SPICAM solar occultations (solid line and error bars showing the measurement uncertainties) and the MGCM (dashed line). The colored zones show the 1-sigma dispersion of the averaged profiles. The 1-sigma dispersions are only calculated for altitudes where at least two profiles were available.

will be the subject of a future paper.

Olsen, K. S. et al. (2020) detected O_3 in the Northern polar regions just before fall equinox (L_s=160-200°) with ACS/ExoMars in MY34. These were the first detections of O_3 in the infrared and revealed the near-surface ozone layer below 30 km down to only a couple of kilometers above the surface. This layer displayed fairly high O_3 concentrations, between 10^9 and 10^{10} cm^{-3}, translating to volume mixing ratios going up to 300 ppm, almost double the values predicted by modeling (Olsen, K. S. et al., 2020). SPICAM has probed the same region during the same season as can be seen in the rightmost panel of Figure 12. The profiles in the latitude band 60-90°N during the season around the equinox (L_s=160-200°) probe altitudes between 10 and 35 km. The average concentration profile measured by SPICAM is between 10^9 and 10^{10} cm^{-3} up to 30 km. These values are consistent with the ACS observations. SPICAM observes quite constant concentrations nearly throughout the profile. The SPICAM statistics are rapidly decreasing below 20 km (only 1-2 profiles available below 22 km), the reason probably being the very difficult detections due to decreasing signal with altitude caused by aerosol extinction, leading to the apparent decrease in concentrations below

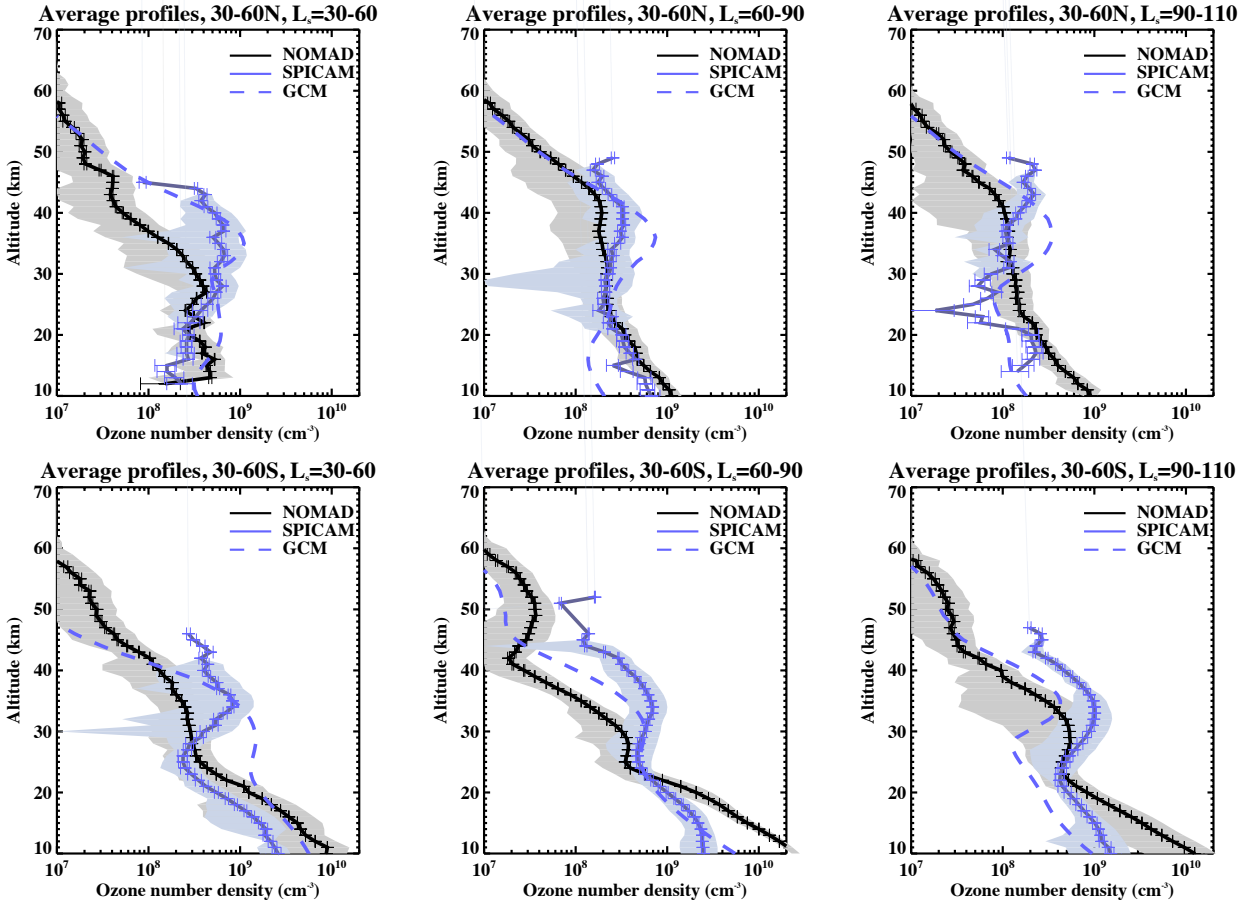

Figure 13: NOMAD-SPICAM comparison at the terminator during the aphelion season. Average ozone concentration profiles (cm^{-3}) as a function of altitude above the areoid for two low-to-midlatitude bands in three L_s intervals at the Northern spring, as marked in the figure. NOMAD (black) and SPICAM (blue) occultations are shown with solid lines with error bars giving the uncertainties of the average and colored zone (NOMAD: grey; SPICAM: blue) showing the 1-sigma dispersion of the averaged profiles. MGCM average profiles are shown with dashed blue line. The 1-sigma dispersions are only calculated for altitudes where at least two data points were available.

15 km in SPICAM profiles.

3.4. Comparison with Nadir and Occultation for MArs Discovery (NOMAD/TGO/ExoMars)

Recently, Patel et al. (2021b) and Khayat et al. (2021) published the first dataset of ozone vertical distribution from Nadir and Occultation for MArs Discovery (NOMAD) solar occultations. We have compared our retrievals to their data in certain zones and seasons in which both datasets contain observations. The two instruments did not observe during the same Mars Years.

The midaltitude aphelion ozone layer is well observed by both instruments in the latitude bands 30-60°N and 30-60°S. The six panels of Figure 13 show average profiles from the two instruments and from the MGCM for these latitude bands and for three L_s ranges. SPICAM concentrations above 30 km are consistently higher than those observed by NOMAD. Below, between 10 and 20 km, it is the inverse: SPICAM concentrations are lower than NOMAD. The model

predicts higher than observed concentrations for the aphelion layer peak in nearly all of the profiles, with the following exceptions. NOMAD peak concentration in the Southern midlatitudes at L_s=90-110° is similar as modeled but slightly lower in altitude (30 km instead of 35 km), whereas SPICAM observes higher than modeled concentrations but with a peak at similar altitudes. In several profiles SPICAM observations are closer to the model in peak concentrations than NOMAD, but the SPICAM peak is less clear and not at the same altitude. Whether or not the differences between SPICAM and NOMAD are due to interannual variability remains to be studied with dedicated modelling that should also be constrained with observed water vapor profiles and dust distributions for the respective years of observations.

We have also compared the two datasets in the polar regions. The southern polar region profiles during the main season of the polar midaltitude ozone layer (L_s=0-90°) are shown in the left panel of Figure 14. NOMAD observes a layer peaking around 48 km altitude with peak concentrations of $5 \cdot 10^7$ cm^{-3}. SPICAM observes even higher values ($9 \cdot 10^7$ cm^{-3}), but the peak altitude is about 5 km below the NOMAD-observed peak. SPICAM detections are scarce above 48 km, inhibiting a full comparison of the profiles. In the lower atmosphere the profiles are in good agreement between 20 and 35 km, with NOMAD showing slightly higher values than the MGCM and SPICAM, but both being within or close to the 1σ variability envelope.

In the Northern polar regions we compare the springtime profiles (L_s=0-90°) as shown in the right panel of Figure 14. The profiles are in good agreement, with SPICAM observing slightly higher concentrations overall, and from 30 to 40 km this difference remains higher than the 1σ variability. The model profile is in between the two observational profiles in this altitude range, agreeing well when accounting for the variability. In the lower atmosphere below 30 km, the model agrees very well with NOMAD whereas SPICAM observes higher values on average but with large variations, the model profile being within the 1σ envelope.

The comparison of the two data sets shows that above 20 km SPICAM is often measuring higher ozone concentrations than NOMAD, whereas below this level SPICAM ozone concentrations are consistently smaller than in NOMAD measurements. The SPICAM detection statistics are the best at altitudes above 20 km. Below 20 km the statistics decrease rapidly since it is very difficult to detect ozone, and this might explain the discrepancy in the lower atmosphere.

4. Conclusions and perspectives

We have analyzed O_3 profiles retrieved from ultraviolet solar and stellar occultations by SPICAM/MEX. Stringent statistical detection criteria were applied to filter out false ozone detections from the dataset. We compared the SPICAM/MEX observations with the LMD Mars GCM. This dataset (2004-2012) complements the previously published SPICAM/MEX O_3 vertical distribution data (Lebonnois et al., 2006; Montmessin and Lefèvre, 2013) and is so far the longest dataset of O_3 vertical distribution on Mars (over four Mars Years). SPICAM observations reported here complement the daytime measurements of $O_2(^1\Delta_g)$ profiles by Clancy et al. (2017) that give insight into the daytime behavior of O_3 vertical distribution.

The observations in low and midlatitudes on both hemispheres map the mid-altitude (30-40 km) O_3 layer during the aphelion season, above the cold and low hygropause. The layer O_3 concentrations are the highest in the latitude range 0-30°S. The layer O_3 concentrations at sunrise/sunset are lower than during the night, due to O_3 photolysis. When compared to the MGCM, the layer concentration peaks are found at similar altitudes (within 5 km) in the data and the model and are overall in fair agreement. Observed and modeled maximum concentrations are mainly within a factor of 2-3. The aphelion ozone layer observations by SPICAM and IUVS/MAVEN (Gröller et al., 2018) agree well despite different years of observation.

In the Southern winter polar vortex, the O_3 layer around 50 km detected in previous studies by Lebonnois et al. (2006); Montmessin and Lefèvre (2013), created by the downward transport of O atoms from the upper atmosphere and forming at the south pole, is observed in its lower part (below 50 km) in our dataset. The observed behavior of the profiles show that the model predicts the layer at higher altitudes than observed. This is also seen in the ozone profile at lower altitudes where the minimum concentrations are also observed lower than the model-predicted minimum, and the lower atmosphere ozone layer top seems to be likewise shifted in altitude.

Solar occultations probed the Northern polar regions, where the model shows fair agreement with the observations. SPICAM also probed the North polar latitudes around the fall equinox at the same season as ACS/ExoMars (although not during the same Martian Year, Olsen, K. S. et al., 2020), and detected similar ozone concentrations below 30 km.

A comparison between NOMAD/TGO and SPICAM occultations, despite the observations being acquired on different Martian Years, reveals a fairly good agreement, when taking into account the variability in the profiles.

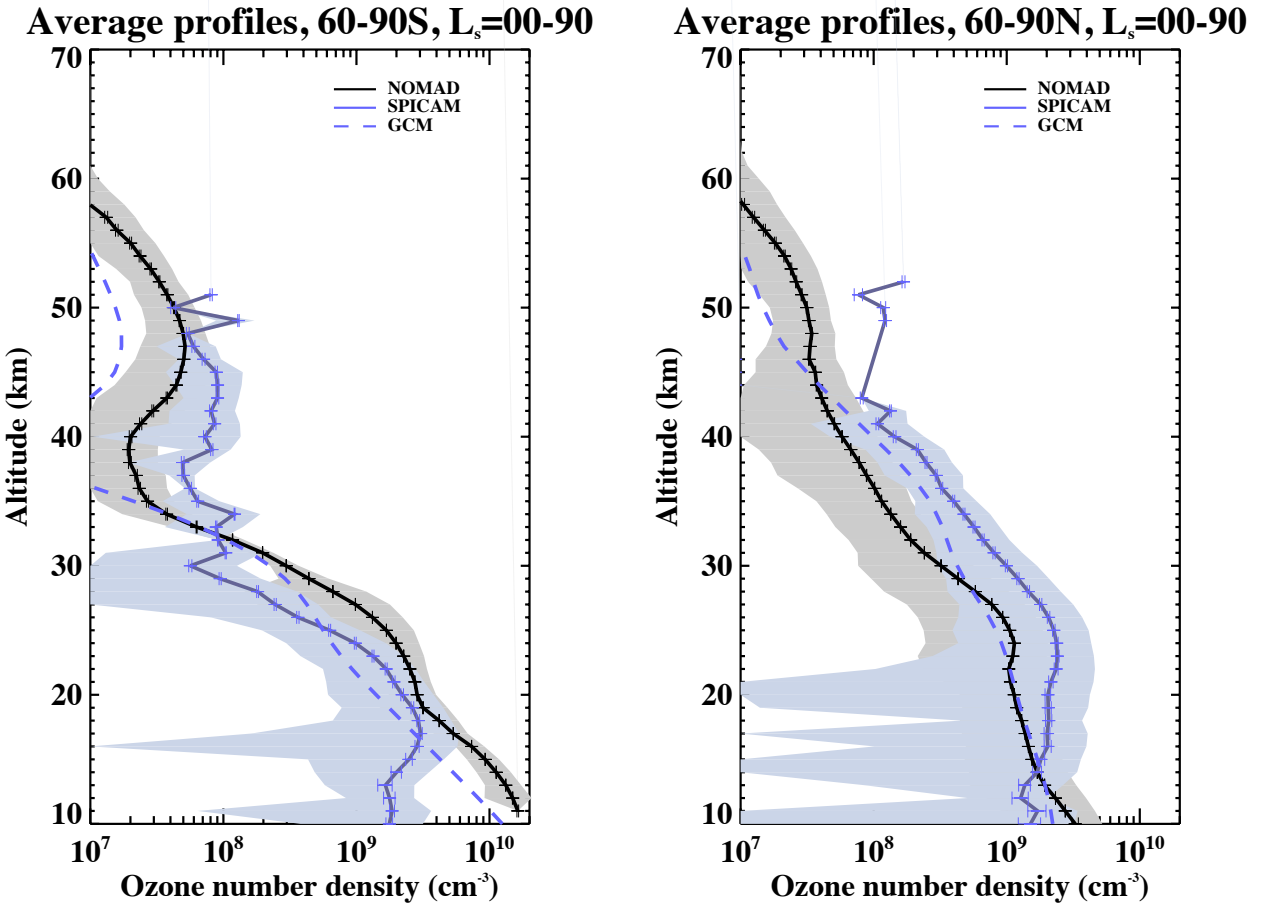

Figure 14: NOMAD-SPICAM comparison in the South Pole. Average ozone concentration profiles (cm^{-3}) as a function of altitude above the areoid for the Southern polar region for the fall-winter season (L_s=0-90∘). NOMAD (black) and SPICAM (blue) occultations are shown with solid lines with error bars giving the uncertainties of the average and colored zone (NOMAD: grey; SPICAM: blue) showing the 1-sigma dispersion of the averaged profiles. MGCM average profiles are shown with dashed blue line. The 1-sigma dispersions are only calculated for altitudes where at least two data points were available.

Quantitatively, SPICAM ozone concentrations are in general higher than the NOMAD-measured ones above 20-30 km in the aphelion ozone layer and in the northern polar regions. At lower altitudes, SPICAM measures smaller concentrations, but the data availability at low altitudes is limited in SPICAM observations.

All of the individual O_3 concentration profiles published in this paper are available at the IPSL ESPRI data center (see Data availability for details).

Acknowledgments

This work was supported by the CNES. It is based on observations with SPICAM embarked on Mars Express. We also acknowledge support from the Programme national de planétologie PNP and the European Union's Horizon 2020 Programme (H2020-Compet-08-2014) under grant agreement UPWARDS-633127.

Data availability

The SPICAM data are available at the European Space Agency's Planetary Science Archive: https://archives.esac.esa.int/psa/

The full O_3 profile dataset is available at the IPSL ESPRI data center: https://doi.org/10.14768/c155973b-c810-4917-b98e-f4d905ed4fc1

The NOMAD ozone dataset was downloaded from Patel et al. (2021a).

Author's Note

This paper replaces the previously withdrawn paper Määttänen et al. (2019). The paper was withdrawn after the discovery of erroneous detections of ozone, biasing the analysis. The current paper has successfully identified these false detections with strict statistical criteria and is thus the reference paper for SPICAM ozone vertical distribution. The withdrawn paper should not be cited.

References

Barth, C.A., Hord, C.W., 1971. Mariner Ultraviolet Spectrometer: Topography and Polar Cap. Science 173, 197–201. doi:10.1126/science.173.3993.197.

Barth, C.A., Hord, C.W., Stewart, A.I., Lane, A.L., Dick, M.L., Anderson, G.P., 1973. Mariner 9 Ultraviolet Spectrometer Experiment: Seasonal Variation of Ozone on Mars. Science 179, 795–796. doi:10.1126/science.179.4075.795.

Bertaux, J., Korablev, O., Perrier, S., Quémerais, E., Montmessin, F., Leblanc, F., Lebonnois, S., Rannou, P., Lefèvre, F., Forget, F., Fedorova, A., Dimarellis, E., Reberac, A., Fonteyn, D., Chaufray, J.Y., Guibert, S., 2006. SPICAM on Mars Express: Observing modes and overview of UV spectrometer data and scientific results. Journal of Geophysical Research (Planets) 111, 10–+. doi:10.1029/2006JE002690.

Blamont, J.E., Chassefiere, E., 1993. First detection of ozone in the middle atmosphere of Mars from solar occultation measurements. Icarus 104, 324–336. doi:10.1006/icar.1993.1104.

Burkholder, J.B., Sander, S.P., Abbatt, J., Barker, J.R., Huie, R.E., Kolb, C.E., Kurylo, M.J., Orkin, V.L., Wilmouth, D.M., Wine, P.H., 2015. Chemical kinetics and photochemical data for use in atmospheric studies, evaluation no. 18. JPL Publication 15-10, Jet Propulsion Laboratory, Pasadena Http://jpldataeval.jpl.nasa.gov/.

Cariolle, D., Moinat, P., Teyssèdre, H., Giraud, L., Josse, B., Lefèvre, F., 2017. Asis v1.0: an adaptive solver for the simulation of atmospheric chemistry. Geosci. Model Dev. 10, 1467–1485. URL: https://www.geosci-model-dev.net/10/1467/2017/, doi:10.5194/gmd-10-1467-2017.

Clancy, R., Sandor, B., Moriarty-Schieven, G., 2004. A measurement of the 362 GHz absorption line of mars atmospheric H_2O_2. Icarus 168, 116 – 121. URL: http://www.sciencedirect.com/science/article/pii/S0019103503004238, doi:https://doi.org/10.1016/j.icarus.2003.12.003.

Clancy, R.T., Nair, H., 1996. Annual (perihelion-aphelion) cycles in the photochemical behavior of the global Mars atmosphere. J. Geophys. Res. 101, 12785–12790. doi:10.1029/96JE00836.

Clancy, R.T., Sandor, B.J., Wolff, M.J., Smith, M.D., Lefévre, F., Madeleine, J.B., Forget, F., Murchie, S.L., Seelos, F.P., Seelos, K.D., Nair, H., Toigo, A.D., Humm, D., Kass, D.M., Kleinböhl, A., Heavens, N., 2013. Correction to "extensive MRO CRISM observations of 1.27 μm o_2 airglow in Mars polar night and their comparison to MRO MCS temperature profiles and LMD GCM simulations". Journal of Geophysical Research: Planets 118, 1148–1154. URL: https://agupubs.onlinelibrary.wiley.com/doi/abs/10.1002/jgre.20073, doi:https://doi.org/10.1002/jgre.20073, arXiv:https://agupubs.onlinelibrary.wiley.com/doi/pdf/10.1002/jgre.20073.

Clancy, R.T., Smith, M.D., Lefèvre, F., McConnochie, T.H., Sandor, B.J., Wolff, M.J., Lee, S.W., Murchie, S.L., Toigo, A.D., Nair, H., Navarro, T., 2017. Vertical profiles of mars 1.27 μm o_2 dayglow from MRO CRISM limb spectra: Seasonal/global behaviors, comparisons to LMD GCM simulations, and a global definition for Mars water vapor profiles. Icarus 293, 132 – 156. URL: http://www.sciencedirect.com/science/article/pii/S0019103516307217, doi:https://doi.org/10.1016/j.icarus.2017.04.011.

Clancy, R.T., Wolff, M.J., Lefèvre, F., Cantor, B.A., Malin, M.C., Smith, M.D., 2016. Daily global mapping of Mars ozone column abundances with MARCI UV band imaging. Icarus 266, 112 – 133. URL: http://www.sciencedirect.com/science/article/pii/S0019103515005266, doi:https://doi.org/10.1016/j.icarus.2015.11.016.

Dubovik, O., Smirnov, A., Holben, B.N., King, M.D., Kaufman, Y.J., Eck, T.F., Slutsker, I., 2000. Accuracy assessments of aerosol optical properties retrieved from Aerosol Robotic Network (AERONET) Sun and sky radiance measurements. J. Geophys. Res. 105, 9791–9806. doi:10.1029/2000JD900040.

Encrenaz, T., Bézard, B., Greathouse, T., Richter, M., Lacy, J., Atreya, S., Wong, A., Lebonnois, S., Lefèvre, F., Forget, F., 2004. Hydrogen peroxide on mars: evidence for spatial and seasonal variations. Icarus 170, 424 – 429. URL: http://www.sciencedirect.com/science/article/pii/S0019103504001654, doi:https://doi.org/10.1016/j.icarus.2004.05.008.

Forget, F., Hourdin, F., Fournier, R., Hourdin, C., Talagrand, O., Collins, M., Lewis, S.R., Read, P.L., Huot, J.P., 1999. Improved general circulation models of the martian atmosphere from the surface to above 80 km. J. Geophys. Res. 104, 24155–24176.

Forget, F., Montmessin, F., Bertaux, J.L., González-Galindo, F., Lebonnois, S., Quémerais, E., Reberac, A., Dimarellis, E., López-Valverde, M.A., 2009. The density and temperatures of the upper martian atmosphere measured by stellar occultations with Mars Express SPICAM. J. Geophys. Res. 114, E01004. Doi:10.1029/2008JE003086.

Gröller, H., Montmessin, F., Yelle, R.V., Lefèvre, F., Forget, F., Schneider, N.M., Koskinen, T.T., Deighan, J., Jain, S.K., 2018. MAVEN/IUVS Stellar Occultation Measurements of Mars Atmospheric Structure and Composition. J. Geophys. Res. 123, 1449–1483. URL: https://agupubs.onlinelibrary.wiley.com/doi/abs/10.1029/2017JE005466, doi:10.1029/2017JE005466, arXiv:https://agupubs.onlinelibrary.wiley.com/doi/pdf/10.1029/2017JE005466.

Guslyakova, S., Fedorova, A., Lefèvre, F., Korablev, O., Montmessin, F., Bertaux, J.L., 2014. O2(a1dg) dayglow limb observations on mars by spicam ir on mars-express and connection to water vapor distribution. Icarus 239, 131–140. URL: https://www.sciencedirect.com/science/article/pii/S0019103514002930, doi:https://doi.org/10.1016/j.icarus.2014.05.040.

Khayat, A.S.J., Smith, M.D., Wolff, M., Daerden, F., Neary, L., Patel, M.R., Piccialli, A., Vandaele, A.C., Thomas, I., Ristic, B., Mason, J., Willame, Y., Depiesse, C., Bellucci, G., López-Moreno, J.J., 2021. ExoMars TGO/NOMAD-UVIS Vertical Profiles of Ozone: 2. The High-Altitude Layers of Atmospheric Ozone. Journal of Geophysical Research: Planets 126, e2021JE006834. URL: https://agupubs.onlinelibrary.wiley.com/doi/abs/10.1029/2021JE006834, doi:https://doi.org/10.1029/2021JE006834, arXiv:https://agupubs.onlinelibrary.wiley.com/doi/pdf/10.1029/2021JE006834. e2021JE006834 2021JE006834.

Krasnopolsky, V., Parshev, V., 1979. Ozone and photochemistry of the martian lower atmosphere. Planetary and Space Science 27, 113 – 120. URL: http://www.sciencedirect.com/science/article/pii/0032063379900400, doi:https://doi.org/10.1016/0032-0633(79)90040-0.

Lebonnois, S., Quémerais, E., Montmessin, F., Lefevre, F., Perrier, S., Bertaux, J.L., Forget, F., 2006. Vertical distribution of ozone on Mars as measured by SPICAM/Mars Express using stellar occultation. Journal of Geophysical Research 111, E09S05. Doi:10.1029/2005JE002643.

Lefèvre, F., Krasnopolsky, V., 2017. Atmospheric Photochemistry. pp. 374–404. doi:10.1017/9781139060172.013.

Lefèvre, F., Lebonnois, S., Montmessin, F., Forget, F., 2004. Three-dimensional modeling of ozone on Mars. J. Geophys. Res. 109, E07004. Doi:10.1029/2004JE002268.

Lefèvre, F., Trokhimovskiy, A., Fedorova, A., Baggio, L., Lacombe, G., Määttänen, A., Bertaux, J.L., Forget, F., Millour, E., Venot, O., Bénilan, Y., Korablev, O., Montmessin, F., 2021. Relationship between the ozone and water vapor columns on Mars as observed by SPICAM and calculated by a Global Climate Model. Journal of Geophysical Research: Planets 126, e2021JE006838. URL: https://agupubs.onlinelibrary.wiley.com/doi/abs/10.1029/2021JE006838, doi:https://doi.org/10.1029/2021JE006838, arXiv:https://agupubs.onlinelibrary.wiley.com/doi/pdf/10.1029/2021JE006838. e2021JE006838 2021JE006838.

Määttänen, A., Listowski, C., Montmessin, F., Maltagliati, L., Reberac, A., Joly, L., Bertaux, J.L., 2013. A complete climatology of the aerosol vertical distribution on Mars from MEx/SPICAM UV solar occultations. Icarus 223, 892–941. doi:10.1016/j.icarus.2012.12.001.

Madeleine, J.B., Forget, F., Millour, E., Navarro, T., Spiga, A., 2012. The influence of radiatively active water ice clouds on the martian climate. Geophys. Res. Lett. 39. URL: https://agupubs.onlinelibrary.wiley.com/doi/abs/10.1029/2012GL053564, doi:10.1029/2012GL053564.

Montabone, L., Forget, F., Millour, E., Wilson, R., Lewis, S., Cantor, B., Kass, D., Kleinböhl, A., Lemmon, M., Smith, M., Wolff, M., 2015. Eight-year climatology of dust optical depth on Mars. Icarus 251, 65–95. URL: https://www.sciencedirect.com/science/article/pii/S0019103515000044, doi:https://doi.org/10.1016/j.icarus.2014.12.034. dynamic Mars.

Montmessin, F., Korablev, O., Lefèvre, F., Bertaux, J.L., Fedorova, A., Trokhimovskiy, A., Chaufray, J., Lacombe, G., Reberac, A., Maltagliati, L., Willame, Y., Guslyakova, S., Gérard, J.C., Stiepen, A., Fussen, D., Mateshvili, N., Määttänen, A., Forget, F., Witasse, O., Leblanc, F., Vandaele, A., Marcq, E., Sandel, B., Gondet, B., Schneider, N., Chaffin, M., Chapron, N., 2017. SPICAM on Mars Express: A 10 year in-depth survey of the Martian atmosphere. Icarus 297, 195 – 216. URL: http://www.sciencedirect.com/science/article/pii/S0019103516308272, doi:https://doi.org/10.1016/j.icarus.2017.06.022.

Montmessin, F., Lefèvre, F., 2013. Transport-driven formation of a polar ozone layer on Mars. Nature Geoscience 6, 930–933. doi:10.1038/ngeo1957.

Montmessin, F., Quémerais, E., Bertaux, J.L., Korablev, O., Rannou, P., Lebonnois, S., 2006. Stellar occultations at UV wavelengths by the SPICAM instrument: Retrieval and analysis of Martian haze profiles. J. Geophys. Res. 111, E09S09. Doi:10.1029/2005JE002662.

Munoz, A.G., McConnell, J., McDade, I., Melo, S., 2005. Airglow on Mars: Some model expectations for the OH Meinel bands and the O_2 IR atmospheric band. Icarus 176, 75 – 95. URL: http://www.sciencedirect.com/science/article/pii/S0019103505000278, doi:https://doi.org/10.1016/j.icarus.2005.01.006.

Määttänen, A., Lefèvre, F., Montmessin, F., Listowski, C., Guilbon, S., Fedorova, A., Korablev, O., 2019. Withdrawn: Climatology of the ozone vertical distribution on Mars from SPICAM/MEX UV occultations. Icarus , 113428URL: https://www.sciencedirect.com/science/article/pii/S0019103518307917, doi:https://doi.org/10.1016/j.icarus.2019.113428.

Navarro, T., Madeleine, J.B., Forget, F., Spiga, A., Millour, E., Montmessin, F., Määttänen, A., 2014. Global climate modeling of the martian water cycle with improved microphysics and radiatively active water ice clouds. J. Geophys. Res. 119, 1479–1495. Doi:10.1002/2013JE004550.

Olsen, K. S., Lefèvre, F., Montmessin, F., Trokhimovskiy, A., Baggio, L., Fedorova, A., Alday, J., Lomakin, A., Belyaev, D. A., Patrakeev, A., Shakun, A., Korablev, O., 2020. First detection of ozone in the mid-infrared at Mars: implications for methane detection. A&A 639, A141. URL: https://doi.org/10.1051/0004-6361/202038125, doi:10.1051/0004-6361/202038125.

O'Neill, N., Royer, A., 1993. Extraction of bimodal aerosol-size distribution radii from spectral and angular slope (Angstrom) coefficients. Applied Optics 32, 1642–1645.

Patel, M., Mason, J., Sellers, G., Holmes, J., Streeter, P., 2021a. NOMAD-UVIS ozone and aerosol vertical profile retrievals for Mars Year 34-35. URL: https://ordo.open.ac.uk/articles/dataset/NOMAD-UVIS_ozone_vertical_profile_retrievals_for_Mars_Year_34-35/13580336/2, doi:10.21954/ou.rd.13580336.v2.

Patel, M.R., Sellers, G., Mason, J.P., Holmes, J.A., Brown, M.A.J., Lewis, S.R., Rajendran, K., Streeter, P.M., Marriner, C., Hathi, B.G., Slade, D.J., Leese, M.R., Wolff, M.J., Khayat, A.S.J., Smith, M.D., Aoki, S., Piccialli, A., Vandaele, A.C., Robert, S., Daerden, F., Thomas, I.R., Ristic, B., Willame, Y., Depiesse, C., Bellucci, G., Lopez-Moreno, J.J., 2021b. ExoMars TGO/NOMAD-

UVIS Vertical Profiles of Ozone: 1. Seasonal Variation and Comparison to Water. Journal of Geophysical Research: Planets 126, e2021JE006837. URL: https://agupubs.onlinelibrary.wiley.com/doi/abs/10.1029/2021JE006837, doi:https://doi.org/10.1029/2021JE006837, arXiv:https://agupubs.onlinelibrary.wiley.com/doi/pdf/10.1029/2021JE006837. e2021JE006837 2021JE006837.

Perrier, S., Bertaux, J.L., Lefevre, F., Lebonnois, S., Korablev, O., Fedorova, A., Montmessin, F., 2006. Global distribution of total ozone on Mars from SPICAM/MEX UV measurements. Journal of Geophysical Research 111, E09S06. Doi:10.1029/2006JE002681.

Piccialli, A., Vandaele, A., Trompet, L., Neary, L., Viscardy, S., Erwin, J., Määttänen, A., Daerden, F., Willame, Y., Robert, S., Aoki, S., Wilquet, V., Lefèvre, F., Montmessin, F., 2021. Impact of gradients at the martian terminator on the retrieval of ozone from SPICAM/MEx. Icarus 353, 113598. URL: https://www.sciencedirect.com/science/article/pii/S0019103519302921, doi:https://doi.org/10.1016/j.icarus.2019.113598. from Mars Express to Exomars.

Quémerais, E., Bertaux, J., Korablev, O., Dimarellis, E., Cot, C., Sandel, B.R., Fussen, D., 2006. Stellar occultations observed by SPICAM on Mars Express. Journal of Geophysical Research (Planets) 111, 9–+. doi:10.1029/2005JE002604.

Willame, Y., Vandaele, A.C., Depiesse, C., Lefèvre, F., Letocart, V., Gillotay, D., Montmessin, F., 2017. Retrieving cloud, dust and ozone abundances in the Martian atmosphere using SPICAM/UV nadir spectra. Planetary and Space Science 142, 9–25. doi:10.1016/j.pss.2017.04.011.